

1 **Numerical Modelling of Coupled Climate, Tectonics and Surface Processes on the**  
2 **Eastern Himalayan Syntaxis**

3 **Xueyun Lu<sup>1</sup>, Jingtao Lai<sup>2</sup>, Lining Wang<sup>3,4</sup>, Jianqing Ji<sup>1</sup>, Dalai Zhong<sup>5</sup>**

4 <sup>1</sup>Key Laboratory of Orogenic Belts and Crustal Evolution, School of Earth and Space Sciences,  
5 Peking University, Beijing 100871, China

6 <sup>2</sup>Earth Surface Process Modelling, GFZ German Research Centre for Geosciences, 14473  
7 Potsdam, Germany

8 <sup>3</sup>Research Institute of Petroleum Exploration & Development, PetroChina, Beijing 100083,  
9 China

10 <sup>4</sup>Key Laboratory of Basin Structure & Hydrocarbon Accumulation, CNPC, Beijing 100083,  
11 China

12 <sup>5</sup>Institute of Geology and Geophysics, Chinese Academy of Sciences, Beijing 100029, China

13

14 Corresponding author: Jianqing Ji ([grsange@pku.edu.cn](mailto:grsange@pku.edu.cn))

15

16 **Key Points:**

- 17 • A climatic-geomorphological-thermomechanical modelling technique is developed to  
18 investigate the evolution of orogenic wedges.
- 19 • The evolution of a specific orogenic wedge primarily relies on the relative strength of  
20 tectonic and climatic forces.
- 21 • The formation of the eastern Himalayan syntaxis results from the cooperation of tectonic  
22 forces, climatic forces and geothermal field.

## 23 **Abstract**

24 The interactions between climate, tectonics and surface processes have become a research  
25 hotspot in Earth science in recent years. Although various insights have been achieved, the  
26 relative importance of climatic and tectonic forcing in influencing the evolution of mountain  
27 belts still remains controversial. In order to investigate the tectonic and topographic evolution, as  
28 well as the formation mechanism of the eastern Himalayan syntaxis, we developed a  
29 comprehensive 2D climatic-geomorphological-thermomechanical numerical model and  
30 conducted over 200 experiments to test the influences of convergence rate, average precipitation  
31 and initial geothermal gradient on orogenic wedge. The results indicate that, for a specific  
32 orogenic wedge, its tectonic and topographic evolution primarily relies on the relative strength of  
33 tectonic and climatic forces, rather than their respective magnitudes. A syntaxis is the result of  
34 the combined effects of tectonic forces, climatic forces and geothermal field. In mountain belts,  
35 once the convergence rate and average precipitation fall within a Type D zone determined by the  
36 crustal thermal structure, a sustained, stationary, localized and relatively rapid erosion process  
37 will be established on the windward flank of the orogenic wedge. This will further induce  
38 sustained and rapid uplift of rocks, exhumation and deformation, ultimately forming a syntaxis.  
39 In this context, syntaxis is the inevitable system's outcome under various physical laws,  
40 including conservation of mass, momentum and energy, rheology, orographic precipitation,  
41 surface processes, etc. Orogens are best viewed as complex open systems controlled by multiple  
42 factors, none of which can be considered as the sole cause of the system's outcome.

43

## 44 **Plain Language Summary**

45 The eastern Himalayan syntaxis is essentially a large-scale antiform, where extreme relief, deep  
46 exhumation, intense deformation, and a steepening near-surface thermal gradient coincide in  
47 core areas. Despite its significance, the formation mechanism of this antiform still remains  
48 controversial. To investigate its formation mechanism, we developed a numerical model that  
49 integrates rock deformation processes, surface processes, and topography-dependent  
50 precipitation. We designed and conducted numerical experiments to investigate the influences of  
51 convergence rate, average precipitation and initial geothermal gradient on the evolution of an  
52 orogenic wedge. The results show that the tectonic and topographic evolution of an orogenic  
53 wedge, as well as the formation of the eastern Himalayan syntaxis, is the result of cooperation of  
54 tectonic compression, precipitation and geothermal field.

## 55 **1 Introduction**

56 The topography of collisional mountain ranges is controlled by both tectonics and climate:  
57 crustal thickening generates topography, while climate modulates surface processes and lowers  
58 mountain heights (Champagnac et al., 2012; Champagnac et al., 2014; Molnar, 2003; Molnar &  
59 England, 1990; Valla et al., 2021; Whipple, 2009; Willett, 2006). Much effort has been made to  
60 understand the mechanisms of the interactions between climate, tectonics and surface processes  
61 through various methods, including analytical treatment (Dahlen, 1990; Dahlen et al., 1988;  
62 Hilley et al., 2004; Roe et al., 2006; Roe et al., 2008; Tomkin & Roe, 2007; Whipple & Meade,  
63 2006), numerical modelling (Avouac & Burov, 1996; Bahadori et al., 2022; Beaumont et al.,  
64 2001; Beaumont et al., 2004; Cruz et al., 2010; Koons et al., 2002; Simpson, 2004; Stolar et al.,  
65 2006; Willett, 1999; Wolf et al., 2022) and field observation (Berger et al., 2008; Clift et al.,

66 2020; Gong et al., 2015; Grujic et al., 2006; Molnar & England, 1990; Norton & Schlunegger,  
67 2011; Peizhen et al., 2001; Reiners et al., 2003; Steer et al., 2014; Tu et al., 2015; Willett et al.,  
68 2006; Ye et al., 2022; Zeitler, Koons, et al., 2001; Zeitler et al., 2014), and many important  
69 insights have been achieved (e.g., NASEM, 2020; Whipple, 2009). For instance, previous  
70 researchers have found that the width and relief of a steady-state critical wedge are quantitatively  
71 related to precipitation and accretionary flux (Roe et al., 2006; Tomkin & Roe, 2007). Surface  
72 processes can influence the tectonic evolution of mountain belts by altering the distribution of  
73 mass on the surface and influencing gravitational stresses (Willett, 2006). Numerical modelling  
74 studies have demonstrated that erosion can promote localized crustal shortening and contribute to  
75 mountain growth (Avouac & Burov, 1996). Additionally, asymmetric rainfall intensity and  
76 erosional efficiency can lead to asymmetric development of the topography, deformation and  
77 exhumation (Willett, 1999). In the case of large, hot orogens like the Himalayan-Tibetan system,  
78 rapid erosion along the plateau margin can facilitate the extrusion of low-viscosity material from  
79 beneath the plateau (Beaumont et al., 2001). However, the relative importance of climatic and  
80 tectonic forcings in influencing the evolution of mountain belts is still debated (Burbank et al.,  
81 2003; Dadson et al., 2003; Herman et al., 2013; King et al., 2016; Molnar, 2003, 2009; Molnar &  
82 England, 1990; Pinter & Brandon, 1997; Raymo & Ruddiman, 1992; Wang et al., 2014;  
83 Whipple, 2009, 2014; Zeitler et al., 2014).

84 In the eastern Himalayan syntaxis, the intense tectonism, heavy precipitation, and ultra-fast  
85 surface processes make it an ideal natural laboratory for investigating the interactions among  
86 tectonics, climate, and surface processes (Bracciali et al., 2016; Gong et al., 2015; Tu et al.,  
87 2015; Yu et al., 2011). On the whole, the eastern Himalayan syntaxis is a large-scale antiform,  
88 in the core areas of which, extreme relief, deep exhumation, intense deformation and steepening  
89 of the near-surface thermal gradient overlap spatially (Burg et al., 1998; Butler, 2019; Koons et  
90 al., 2013; Zeitler et al., 2014). Various models have been proposed to illustrate its formation  
91 mechanism and structural evolution (Butler et al., 2002; Ding et al., 2001; Koons, 1995;  
92 Mukhopadhyay et al., 2011; Whipp Jr et al., 2014; Zeitler, Koons, et al., 2001). Classical models  
93 include northward indentation of Indian plate (Ding et al., 2001; Koons, 1995; Zhang et al.,  
94 2004), crustal and lithospheric scale folding under continental shortening (Burg et al., 1998;  
95 Burg & Podladchikov, 1999; Burg et al., 1997) and tectonic aneurysm (Koons et al., 2013;  
96 Zeitler, Koons, et al., 2001; Zeitler, Meltzer, et al., 2001). Concretely, the indentation model  
97 posits that syntaxis results from the northward indentation of the Indian continental indenter,  
98 while the crustal and lithospheric scale folding model believes that the large-scale antiform arises  
99 from lithospheric buckling, which is considered as a basic response to large-scale continental  
100 shortening. The tectonic aneurysm model attributes the development of the syntaxis to the  
101 positive feedbacks among erosion, heat advection, rock strength, and deformation. These models  
102 focus on different factors. For instance, the indentation model highlights the influences of plate  
103 geometry and rock strength, while the crustal and lithospheric scale folding model emphasizes  
104 the role of tectonic forces. The tectonic aneurysm model assigns a crucial role to climate and  
105 surface processes. Nevertheless, extensive research has demonstrated that climatic forces,  
106 tectonic forces and rock strength (crustal thermal structure) all play crucial roles in influencing  
107 the evolution of an orogenic wedge (Avouac & Burov, 1996; Beaumont et al., 2001; Buitter,  
108 2012; Royden et al., 2008; Ruh et al., 2012; Tapponnier et al., 2001; Vogt et al., 2017; Vogt et  
109 al., 2018; Willett, 1999), and their respective roles (regardless of magnitude) persist throughout  
110 the whole course of orogenesis. When evaluating the impact of one specific factor, it is essential  
111 to consider the other relevant factors as preconditions or assumptions. These models have

112 different preconditions and assumptions, making comparison and testing among them  
113 challenging. Thus, further quantitative research on the feedback mechanisms and the relative  
114 importance of climate and tectonics is required.

115 To quantitatively investigate the interactions between climate, tectonics and surface  
116 processes, as well as the formation conditions and mechanisms of the eastern Himalayan  
117 syntaxis, we developed a comprehensive 2D climatic-geomorphological-thermomechanical  
118 numerical model and conducted a set of experiments to investigate the evolution of orogenic  
119 wedges under varying climatic, tectonic and geothermal conditions. Our results indicate that the  
120 formation of the eastern Himalayan syntaxis is the consequence of the combined effects of  
121 climatic forcing, tectonic forcing and crustal thermal structure (or rock strength).

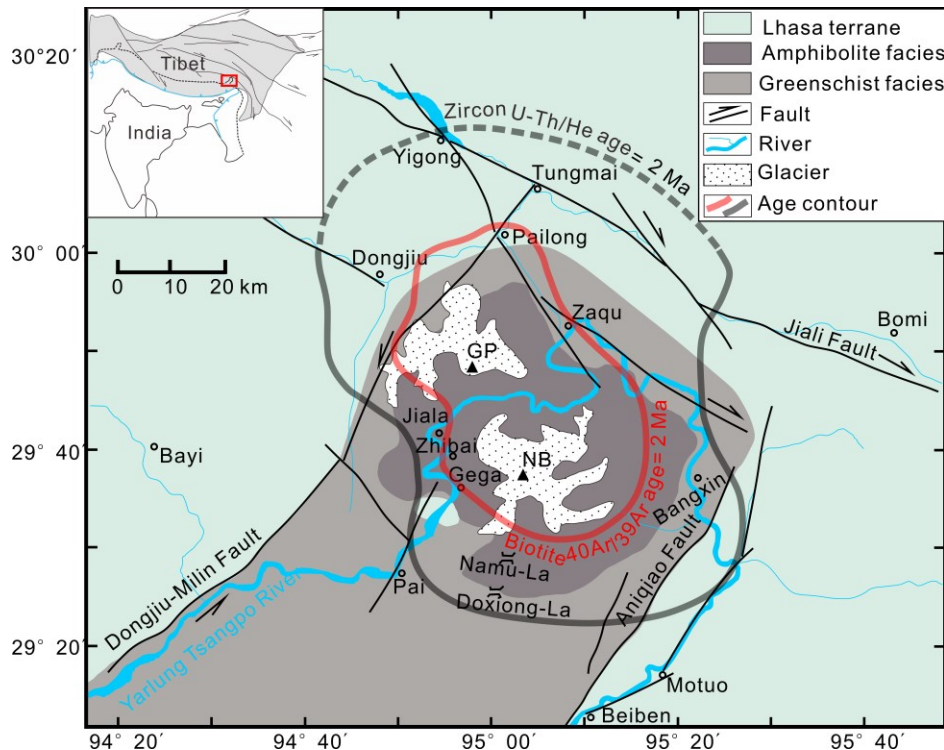
## 122 **2 Background**

123 Located at the eastern end of Himalayan arc, the eastern Himalayan syntaxis is part of the  
124 Himalayan orogenic belt and essentially a special orogenic wedge (Yin, 2006). Compared to the  
125 central Himalayan arc, the eastern Himalayan syntaxis exhibits the following characteristics:  
126 (1)The overall structure exhibits a large-scale antiform (Burg et al., 1998; Burg et al., 1997).  
127 (2)A broad upwarp of the Moho beneath the Namche Barwa, with the crustal thickness in the  
128 core area of the syntaxis (55 km) appearing notably lower than the regional background crustal  
129 thickness (~70 km) (Zeitler et al., 2014). (3) Steep thermal gradients in upper crust (>50 °C/km)  
130 (Craw et al., 2005). (4) Strong “bull’s-eye” spatial localization of deformation (< ~50 km in  
131 diameter) (Bendick & Ehlers, 2014; Koons et al., 2013). (5) The thermochronological ages  
132 generally become younger with proximity to the Namche Barwa Peak (NBP), the core area of the  
133 syntaxis (Gong et al., 2015; King et al., 2016; Tu et al., 2015). (6) Rapid exhumation rate (>5  
134 mm/yr)(Burg et al., 1997; Enkelmann et al., 2011; King et al., 2016; Stewart et al., 2008). (7)  
135 Extreme relief, intense climate and surface processes overlap in local area within the orogenic  
136 belt (Bookhagen & Burbank, 2006; Koons et al., 2013; Yu et al., 2017). Although the collision  
137 of India with Asia has been widely acknowledged to have occurred over 50 million years ago,  
138 many of the significant structures associated with the formation of the eastern Himalayan  
139 syntaxis only formed within the past 10 Myr (Butler, 2019; Zeitler et al., 2014).

### 140 **2.1 Geological setting**

141 The eastern Himalayan syntaxis is Cored by the Namche Barwa-Gyala Peri massif  
142 (NBGPM) and surrounded by the Lhasa terrane to the east, north, and west (Figure 1). In this  
143 region, the Lhasa terrane is mainly composed of high-grade metamorphic rocks, Cambrian–  
144 Eocene unmetamorphosed strata and numerous plutons (Gangdese granites) (Zhang et al., 2010).  
145 The core metamorphic massif primarily consists of meta-sedimentary greenschist-facies schists  
146 and amphibolite- to granulite-facies gneisses. These include garnet biotite schist, biotite epidote  
147 schist, sillimanite garnet biotite gneiss, biotite hornblende plagioclase gneiss, and biotite  
148 plagioclase amphibolites (Tu et al., 2015). High-pressure granulite-facies metamorphic rocks are  
149 predominantly exposed in the core area of the syntaxis, particularly near NBP (Booth et al.,  
150 2009; Ding et al., 2001; Liu & Zhong, 1997; Tu et al., 2015). According to Booth et al. (2009)’s  
151 study, the peak metamorphic pressures and temperatures within the core of the massif are  
152 estimated to be 10~14 kbar and 700~900 °C, respectively. Meanwhile, abundant young  
153 granitoids distribute in the region with the youngest age of only 0.9 Ma being reported (Zeitler et  
154 al., 2014). Geochemical analysis suggests that these young granites within the core of the massif

155 predominantly originate from rapid depression melting of parent rocks (Booth et al., 2004;  
 156 Koons et al., 2013).  
 157



158  
 159 **Figure 1.** Geological sketch of the eastern Himalayan syntaxis showing the main geological  
 160 units and structures (after Tu et al. (2015)). The inset in the top left corner illustrates the location  
 161 of the eastern Himalayan syntaxis within the Himalayan-Tibetan orogenic belt. The bold black  
 162 and red lines outline the areas with previously published young (<2 Ma) zircon U-Th/He and  
 163 biotite 40Ar/39Ar ages, respectively (after Stewart et al. (2008)).  
 164

165 The overall structure of the eastern Himalayan syntaxis is a large NE-trending and N-  
 166 plunging antiform (30 to 40 km wide), with its hinge lying near Doxiong-La (Burg et al., 1998;  
 167 Burg et al., 1997; Ding et al., 2001). To the west of the syntaxis, the left-slip NE-trending  
 168 Donjiu–Milin ductile fault zone defines its western boundary (Zhang et al., 2004), while the dip-  
 169 slip NE-trending ductile Aniqiao fault zone is considered as its eastern bounding structure. To  
 170 the north of the syntaxis lies the nearly E–W-trending Jiali ductile shear zone. The structural data  
 171 suggests that this zone underwent a kinematic shift from left-slip to right-slip during its  
 172 movement history (Lin et al., 2009). There are also a series of 290° - trending right-slip thrust  
 173 fault zones and NE(or NW)-trending high-angle brittle normal faults in the syntaxis (Tu et al.,  
 174 2015; Zhang et al., 2004).

## 175 2.2 Climate and geomorphology

176 Present climate data shows that the precipitation in the Tibetan Plateau is concentrated  
 177 along the southern Himalayan topographic front, while the two ends of the Himalayan arc  
 178 receive the highest amount of precipitation (Bookhagen & Burbank, 2006). According to the  
 179 rainfall amounts estimated from TRMM (Tropical Rainfall Measurement Mission) satellite data,  
 180 the annual average precipitation in the eastern Himalayan syntaxis region is currently around 2

181 m/yr, with maximum rainfall reaching up to 6 m/yr (Anders et al., 2006; Bookhagen & Burbank,  
182 2006). In addition, the NBP and GPP (Gyala Peri Peak) are covered by massive modern glaciers,  
183 with the equilibrium line altitudes (ELAs) ranging between 4400 and 4500 m (Yao et al., 2010).  
184 The presence of abundant moraine deposits and outwash (with thickness ranging from 100 m to  
185 over 200 m) discovered at altitudes of 2900 to 4800 m at the foot of NBP also suggests that the  
186 eastern Himalayan syntaxis region has been subjected to significant glacial activities since  
187 Quaternary (Song et al., 2012).

188 The Yarlung Tsangpo River, the largest river in southern Tibet, flows parallel to the  
189 Himalayan orogenic belt for ~1700 km before entering the eastern Himalayan syntaxis, where it  
190 suddenly becomes narrow and deeply entrenched, creating one of the most spectacular gorges on  
191 the planet, the Yarlung Tsangpo Canyon. At the syntaxis, the river undergoes a rapid turn of  
192 ~180°, giving rise to a topographic relief of nearly 5 km within a horizontal distance of ~12 km.  
193 Then it flows southward, leaving the syntaxis (Finnegan et al., 2008; Yang et al., 2018). Under  
194 the influences of intense climate and tectonism, the eastern Himalayan syntaxis has developed  
195 distinct geomorphic features, including extreme local relief of over 4 km, steep topographic  
196 slopes and towering peak elevations that extend well above the ELA (Koons et al., 2013).

## 197 2.3 Thermochronology

198 The thermochronological ages in the eastern Himalayan syntaxis are relatively young (King  
199 et al., 2016). In this region, the published biotite  $^{40}\text{Ar}/^{39}\text{Ar}$  are basically younger than 8 Ma  
200 (Gong et al., 2015; Stewart et al., 2008; Yu et al., 2011; Zhang et al., 2004). In the center of the  
201 metamorphic massif, some of the biotite  $^{40}\text{Ar}/^{39}\text{Ar}$  ages can be as low as 0.2 and 0.4 Ma  
202 (Zeitler et al., 2014). The reported zircon fission track ages, zircon U-Th/He ages and apatite  
203 fission track ages are generally younger than 3 Ma (Burg et al., 1998; Stewart et al., 2008; Tu et  
204 al., 2015; Yu et al., 2011), while the youngest zircon fission track age and zircon U-Th/He age  
205 can be as low as 0.2 Ma and 0.2~0.3 Ma, respectively (Seward & Burg, 2008; Zeitler et al.,  
206 2014). In contrast, the thermochronological ages of the surrounding Lhasa terrane are relatively  
207 older (Gong et al., 2015; Zeitler et al., 2014). On the whole, the four types of  
208 thermochronological data mentioned above show a gradual decrease in age as they approach the  
209 core area of the syntaxis (Figure 1). All these data suggest rapid exhumation rates in this region.  
210 According to the P-T estimates, U-Pb and Th-Pb dating of metamorphic and anatectic phases, it  
211 is inferred that the long-term (since 5~10 Ma) exhumation rate in the core area of the syntaxis  
212 could reach 4~6 mm/yr or more, with total exhumation exceeding 20 km (Koons et al., 2013).  
213 Enkelmann et al. (2011) also reported decadal erosion rates of 5~17 mm/yr in the region based  
214 on the study of detrital zircon from the Brahmaputra River and tributaries.

## 215 3 Methodology

216 In this study, we use a coupled 2D climatic-geomorphological-thermomechanical modelling  
217 technique to simulate the crustal deformation, geothermal evolution, partial melting, fluvial  
218 erosion, sediment deposition, hillslope, and orographic precipitation in a compressional system.

### 219 3.1 Tectonic processes

220 In the thermomechanical model, the following continuity equation and stokes equation are  
221 employed to approximate the conservation of mass and momentum for 2D incompressible  
222 material in the gravitational field. The geothermal evolution of the system is modelled by solving  
223 the energy equations, which account for radioactive, shear, adiabatic and latent heat production.

224 Incompressible continuity equation:

$$225 \quad \frac{\partial v_x}{\partial x} + \frac{\partial v_y}{\partial y} = 0 \quad (1)$$

226 where  $v_x$  and  $v_y$  are horizontal and vertical velocity components, respectively.

227 2D stokes equation:

$$228 \quad \frac{\partial \sigma'_{ij}}{\partial x_j} - \frac{\partial P}{\partial x_i} + \rho(C, P, T, M)g_i = 0 \quad (2)$$

229 where  $i$  and  $j$  are coordinate indexes,  $x_j$  and  $x_i$  are spatial coordinates,  $\sigma'_{ij}$  is the deviatoric stress  
230 tensor,  $g_i$  is the  $i$ th component of the gravity vector,  $\rho$  is the density, which depends on the  
231 composition ( $C$ ), pressure ( $P$ ), temperature ( $T$ ) and melt fraction ( $M$ ).

232 Energy equations:

233

$$234 \quad \rho C_p \frac{DT}{Dt} = -\frac{\partial q_i}{\partial x_i} + H_r + H_s + H_a + H_L \quad (3)$$

$$235 \quad q_i = -k(C, T) \frac{\partial T}{\partial x_i} \quad (4)$$

$$236 \quad H_a = T \alpha \frac{DP}{Dt} \quad (5)$$

$$237 \quad H_s = \frac{\sigma'_{xx}{}^2}{\eta_{vp}} + \frac{\sigma'_{xy}{}^2}{\eta_{vp}} \quad (6)$$

238 where  $C_p$  is the effective isobaric heat capacity,  $\frac{DT}{Dt}$  is the substantive time derivative of  
239 temperature,  $q_i$  is the heat flux components,  $H_r$ ,  $H_s$ ,  $H_a$  and  $H_L$  are the radioactive, shear,  
240 adiabatic and latent heat production, respectively.  $k(C, T)$  is the composition- and temperature-  
241 dependent thermal conductivity,  $\frac{DP}{Dt}$  is the substantive time derivative of pressure,  $\alpha$  is the  
242 thermal expansion,  $\eta_{vp}$  is the effective visco-plastic viscosity. For details regarding the visco-  
243 elasto-plastic rheology of rocks, the partial melting model, and the material properties used in  
244 this study, readers are referred to Texts S1, S2, and Table S1 in Supporting Information S1.

### 245 3.2 Surface processes

246 Considering the code accessibility, feasibility and brevity, a landscape evolution model that  
247 accounts for the stream-power law (SPL) fluvial erosion, sediment deposition, hillslope, tectonic  
248 horizontal advection and vertical uplift is adopted (Barnhart et al., 2019; Culling, 1963; Davy &  
249 Lague, 2009):

$$250 \quad \frac{\partial h}{\partial t} = \frac{VQ_s}{Q} - KQ^m S^n + K_s \nabla^2 h - \mathbf{v} \cdot \nabla h \quad (7)$$

251 where  $h$  is the topographic elevation,  $t$  is time,  $K_s$  is the ‘topography diffusion’ coefficient,  $K$  is  
252 the erodibility,  $m$  and  $n$  are the discharge and slope exponents, respectively.  $V$  is the effective  
253 settling velocity of the sediment particles,  $\mathbf{v}$  is the material velocity vector at the surface.  $Q$  is  
254 volumetric water discharge,  $Q_s$  is volumetric sediment discharge. The volumetric sediment  
255 discharge at a specific downstream point ( $Q_{s,out}$ ) is determined by integrating all the erosion  
256 minus deposition that has occurred upstream (Barnhart et al., 2019):

$$257 \quad Q_{s,out} = \int_A \left( [KQ^m S^n]_s - \left[ \frac{VQ_s}{Q} \right]_s \right) dA \quad (8)$$

258 Here, the water discharge is calculated based on the orographic precipitation. It has been  
 259 recognized that topography has a profound effect on the spatial patterns of precipitation (Roe,  
 260 2005; Roe et al., 2002; Smith & Barstad, 2004). Mountains can influence the flow of air and  
 261 disturb the vertical stratification of the atmosphere by acting as physical barriers and sources or  
 262 sinks of heat, thereby influencing the patterns of precipitation (Barros & Lettenmaier, 1994). At  
 263 the space scale of mountain ranges (tens to hundreds of kilometers) and in the climatological  
 264 average, the windward flank of the mountain range receives significantly higher precipitation  
 265 compared to the leeward flank, forming the well-known rain shadow. Such precipitation  
 266 localization effect is well observed in mountain ranges in today's climate across a wide range of  
 267 latitudes, such as Southern Alps of New Zealand (Wratt et al., 2000), Himalayas (Bookhagen &  
 268 Burbank, 2006; Burbank et al., 2003), Cascades mountains of Washington (Reiners et al., 2003)  
 269 and St Elias Range of Alaska (Berger & Spotila, 2008). Here, following Anders et al. (2006)'s  
 270 study, we assume that the precipitation in Himalayas is proportional to two factors. One is  
 271 saturation vapor pressure at the surface, and the other is the saturation vapor pressure multiplied  
 272 by the slope of the topography in the direction of the prevailing wind:

$$273 \quad P = (\alpha_p + \beta_p S) e_{sat}(T) \quad (9)$$

274 where  $P$  is precipitation,  $\alpha_p$  and  $\beta_p$  are constants,  $S$  is the topographic slope in the direction of  
 275 the prevailing wind.  $e_{sat}(T)$  is the saturation vapor pressure, and it can be estimated by the  
 276 Clausius-Clapeyron relation (Emanuel, 1994):

$$277 \quad e_{sat}(T) = 6.112 \exp\left(\frac{aT}{b + T}\right) \quad (10)$$

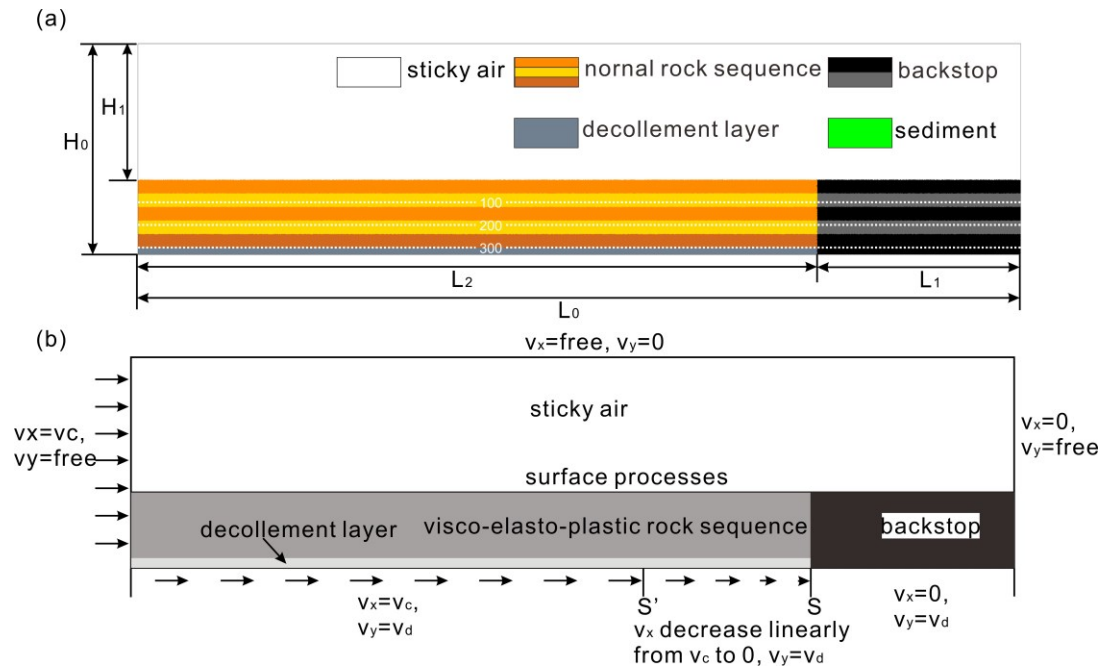
278 where  $a = 17.67$ ,  $b = 243.5^\circ\text{C}$ ,  $T$  is the air temperature in degrees Celsius, and it is calculated  
 279 using an average temperature at sea level ( $T_0$ , assumed to be  $30^\circ\text{C}$ ) and a constant air  
 280 temperature lapse rate ( $\Gamma$ , assumed to be  $-7^\circ\text{C}/\text{km}$ ), expressed as  $T = T_0 + \Gamma h$ .

281 Although its simplicity, this model captures the significant features of the pattern of the  
 282 precipitation in Himalayas (Anders et al., 2006), and it's easy to implement and couple with  
 283 landscape evolution models and thermomechanical models. According to the regression analysis  
 284 by Anders et al. (2006), the values of  $\alpha_p$  and  $\beta_p$  are approximately within the range of 0 to 1,  
 285 and they are region-specific and scale-dependent, which indicates that there is no single set of  
 286 values should be generally applicable. For details regarding the selection of these two  
 287 parameters, readers are referred to Text S3 and Figure S1 in Supporting Information S1.

### 288 3.3 Numerical model design

289 The initial model domain extends 31 km in the Y direction and varies from 600 to 1000 km  
 290 in the X direction depending on the total shortening amount (Figure 2a). To simulate the  
 291 topographic evolution, the top 20 km of the model domain is set as "sticky air" layer with  
 292 viscosity of  $10^{18} \text{ Pa s}$  and density of  $1 \text{ kg/m}^3$  (Cramer et al., 2012; Schmeling et al., 2008).  
 293 Beneath the "sticky air" layer, the rightmost 100 km is set as a relatively rigid backstop, while  
 294 the left part is composed of 11-km-thick undeformed visco-elasto-plastic rock sequence.  
 295 Referring to the seismic reflection profile across Himalayas (Schulte-Pelkum et al., 2005) and  
 296 some general profiles of fold-and-thrust belts or accretionary wedges on the planet (Buiter, 2012;  
 297 Ruh et al., 2012), we assume that the initial thickness of the normal undeformed rock sequence is  
 298 10 km. Beneath this rock sequence, a 1-km-thick decollement layer is introduced to mimic the  
 299 main decollement at the base of Himalayan orogenic wedge. This decollement layer is assumed  
 300 to be frictional and has smaller compressive strength and internal friction coefficient compared  
 301 to the normal rock sequence so that it's prone to plastic deformation (Ruh et al., 2012)(see

302 material properties in Table S1 in Supporting Information S1). The model is solved by  $401 \times 81$   
 303 non-uniform Eulerian nodes, with the finest initial resolution of  $1 \text{ km} \times 0.39 \text{ km}$  in the proximity  
 304 of the convergence center, and 8 million randomly distributed Lagrangian markers.  
 305



306 **Figure 2.** Model setup. (a) Initial model configuration. The definitions of each parameter  
 307 can be found in Table 1. Different colors represent different rock types, with: white—sticky air;  
 308 orange, yellow and brown—normal rock sequence; slategrey—decollement layer; grey and  
 309 black—backstop; green—sediment. The sediment is not shown in Figure 3a, but will appear  
 310 during the evolution of the model. The white dashed lines indicate isotherms (in  $^{\circ}\text{C}$ ). (b)  
 311 Boundary conditions.  $v_c$  represents the convergence rate, and  $v_d$  is defined in the main text.  
 312

313  
 314 To simulate the mechanical environment at convergent plate boundary, a horizontal  
 315 convergence velocity  $v_c$  (towards the right) is applied on the left boundary and the left portion of  
 316 the lower boundary (Figure 2b), while the horizontal velocity on the right boundary and the right  
 317 portion (right side of point S in Figure 2b) of the lower boundary is fixed at zero. To prevent  
 318 abrupt velocity change, the horizontal velocity between S and S' at the lower boundary is  
 319 assumed to decrease linearly from the convergence rate  $v_c$  to zero. In order to ensure mass  
 320 conservation in the computational model, a vertical outward velocity  $v_d = H * v_c / L$ , which  
 321 changes at every time step, is prescribed along the lower boundary. Here,  $H$  and  $L$  are the current  
 322 height and width of the model, respectively. The upper boundary is free slip. All the experiments  
 323 presented here share the same boundary conditions.

324 The thermal boundary conditions are  $0^{\circ}\text{C}$  at the upper boundary and zero heat flux across  
 325 the vertical boundaries. The temperature of the “sticky air” is consistent with temperature at the  
 326 upper boundary. The temperature gradient at the lower boundary is fixed at the initial geothermal  
 327 gradient  $dT/dh$  in order to ensure a relatively stable inward heat flux. The initial geothermal  
 328 field is assumed to increase linearly from  $0^{\circ}\text{C}$  at the surface to a specific bottom temperature,  
 329 which varies depending on the initial geothermal gradient.  
 330

331 **Table 1.** Parameters used in the numerical experiments

Parameter	Description	Value
$H_0$	Height of the initial setup (km)	31
$H_1$	Thickness of the air (km)	20
$L_0$	Initial length of the model (km)	600~1000
$L_1$	Length of backstop (km)	100
$L_2$	Length of rock sequence (km)	500~900
$T_{\text{top}}$	Temperature at model top ( $^{\circ}\text{C}$ )	0
$dT/dh$	Initial thermal gradient ( $^{\circ}\text{C}/\text{km}$ )	10~45 <sup>a</sup>
$P_0$	The average annual precipitation (m/yr)	0~20
$v_c$	Convergence rate (cm/yr)	0.5~5.0
$T_0$	Temperature at sea level in the model of orographic precipitation ( $^{\circ}\text{C}$ )	30
$\Gamma$	The constant lapse rate in the model of orographic precipitation ( $^{\circ}\text{C}/\text{km}$ )	-7.0
$\beta_P$	The coefficient in the model of orographic precipitation	0.370
$V$	effective settling velocity of the sediment particles (m/yr)	1.0 <sup>b</sup>
$K$	the erodibility in the stream-power incision model ( $\text{m}^{-0.5}\text{yr}^{-0.5}$ )	$2 \cdot 10^{-5}$ <sup>c</sup>
$m$	The discharge exponent in the stream-power incision model	0.5 <sup>c</sup>
$n$	The slope exponent in the stream-power incision model	1.0 <sup>c</sup>
$K_s$	the ‘topography diffusion’ coefficient ( $\text{m}^2/\text{yr}$ )	0.035 <sup>d</sup>

332 *Note.* <sup>a</sup> Parameters from (Turcotte & Schubert, 2014). <sup>b</sup> Parameters from Yuan et al. (2019). <sup>c</sup>  
 333 Parameters from Whipple and Tucker (1999). <sup>d</sup> Parameters from Fernandes and Dietrich (1997)

334

335

336

337

338

339

340

341

342

343

344

345

Given that many of the significant structures linked to the development of the eastern Himalayan syntaxis are younger than 10 Ma, we focus our research on the most recent 7 Myr, rather than the entire evolutionary history of the Himalayan-Tibetan orogenic belt since the onset of collision. The total model runtime is set to 8 Myr. The precipitation for the first 1 Myr is set to 0 m/yr to achieve a model state with a certain degree of deformation and relief. The orographic precipitation is applied after  $t=1$  Myr, and for all the experiments, it’s assumed that the direction of the prevailing winds is consistent with the direction of the subduction, which is from the left. By varying the convergence rate  $v_c$ , average precipitation  $P_0$ , and initial geothermal gradient  $dT/dh$ , which is related to the overall strength of the shallow crustal rock sequence, a total of 232 experiments are designed and conducted (Table S2, S3, and S4 in Supporting Information S1).

### 346 3.3 Numerical implementation

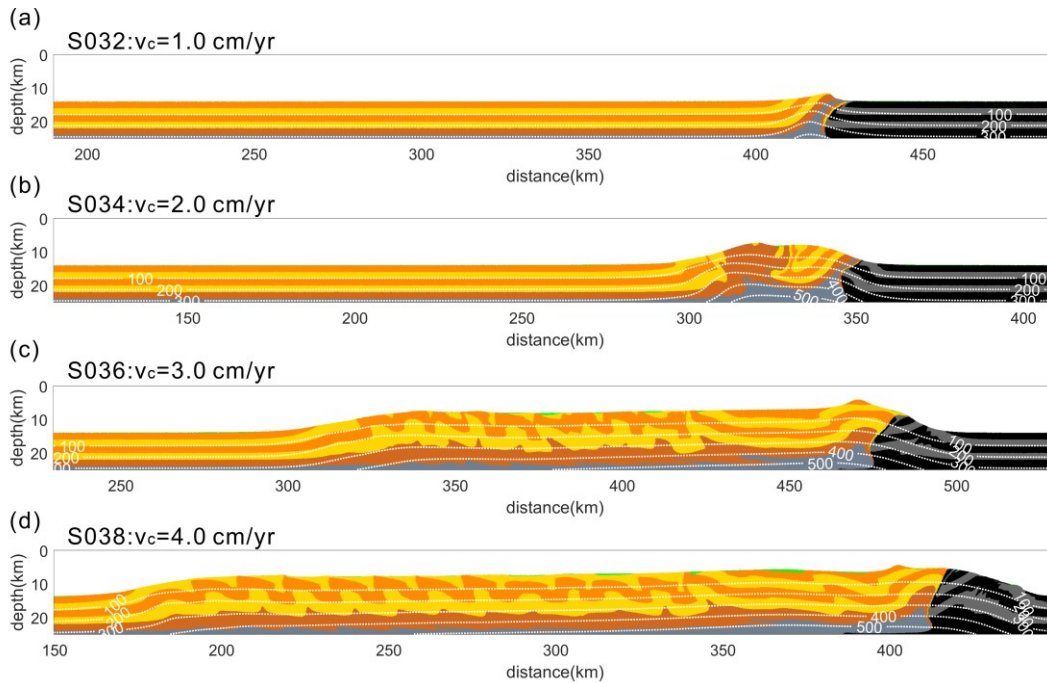
347 The thermomechanical processes are solved using the code provided by Gerya (2019),  
348 which uses a finite difference approach and a marker in cell technique to solve the thermal and  
349 mechanical equations mentioned above. The surface processes and orographic precipitation are  
350 implemented through landlab, an open-source package for numerical modelling of Earth surface  
351 dynamics (Barnhart et al., 2019; Barnhart et al., 2020; Hobley et al., 2017), and Python  
352 programming. We use a 3-by-N regular landlab grid with top and bottom edges as fixed zero  
353 gradient boundaries to simulate the evolution of a 1D model domain. We couple the  
354 thermomechanical model, surface processes model, and orographic precipitation model through  
355 the following steps. Firstly, the thermomechanical processes are solved using the finite  
356 difference code. This provides the current topography, which is then used to simulate the  
357 precipitation based on the orographic precipitation model. Subsequently, the surface processes  
358 are solved based on the topography and precipitation with smaller sub-time steps in landlab, after  
359 which the elevation changes due to surface processes can be determined. Based on these  
360 elevation changes and the thermomechanical velocity field, the topography in the model is  
361 updated. At the same time, if the rock types of the Lagrangian markers near the surface has  
362 changed, the corresponding field quantities are also updated. This process is repeated until the  
363 computation reaches the predetermined end time.

## 364 4 Results

### 365 4.1 Relative importance of tectonic and climatic forcings in controlling the evolution of 366 orogenic wedge

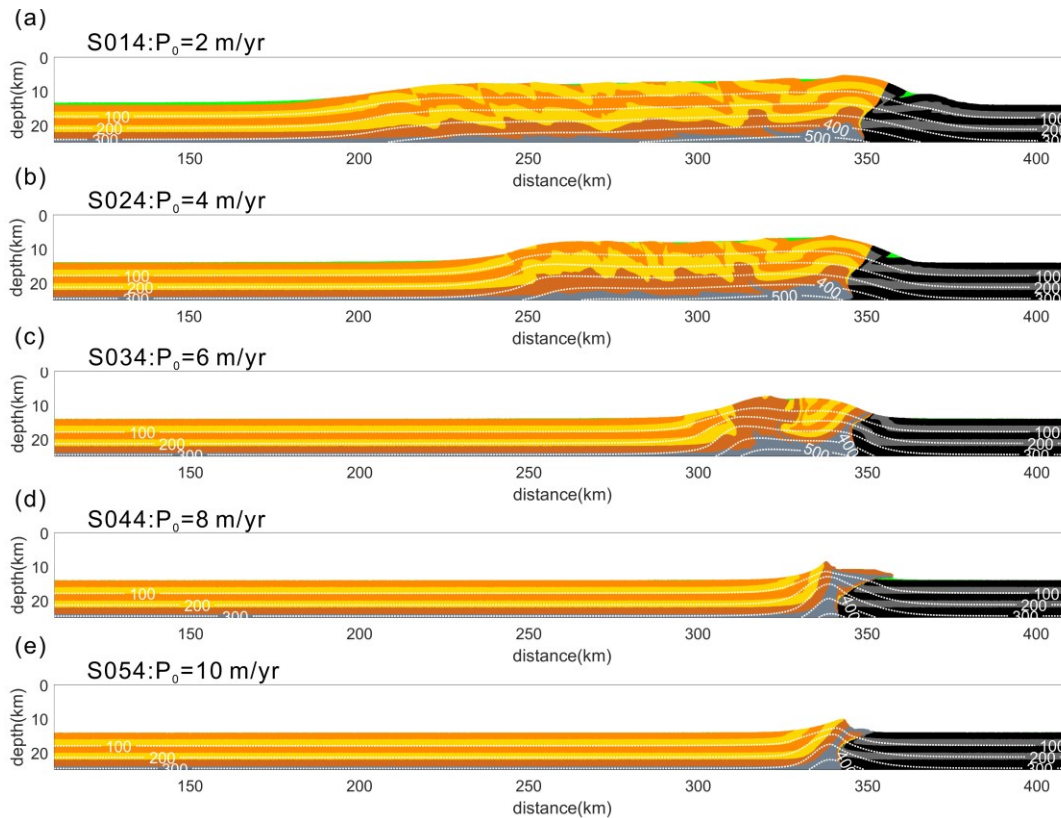
367 The modelling results indicate that the convergence rate, average precipitation and initial  
368 geothermal gradient all have significant influences on the structural and geomorphic evolution of  
369 the orogenic wedge. For all the models depicted in Figure 3 and 4, the initial geothermal  
370 gradients are consistently set at 30 °C/km. When increasing the convergence rate and  
371 maintaining a constant average precipitation, it leads to an increase in the width and height of the  
372 orogenic wedge (Figure 3). Additionally, at relatively lower convergence rates, the orogenic  
373 wedge tends to develop folds or fault-related folds (Figure 3b), and for those models with  
374 sufficiently low convergence rates, the deformation structures and topography will be unable to  
375 withstand intense erosion and thus cannot be completely preserved (Figure 3a). As the  
376 convergence rate increases, the deformation style within the orogenic wedge gradually  
377 transitions to thrust faults, and the deformation continuously extends towards the foreland basin  
378 through developing imbricate structures (Figure 3c and d).

379



380  
 381 **Figure 3.** Numerical modelling results showing the influence of convergence rate ( $v_c$ ) on the  
 382 evolution of orogenic wedges. The white dashed lines indicate isotherms (in  $^{\circ}\text{C}$ ). For all models,  
 383 the average precipitation ( $P_0$ ) is 6 m/yr, the initial geothermal gradient ( $dT/dh$ ) is  $30\text{ }^{\circ}\text{C}/\text{km}$ , and  
 384 the runtime is 8 Myr. The convergence rates for (a), (b), (c) and (d) are 1.0 cm/yr, 2.0 cm/yr, 3.0  
 385 cm/yr and 4.0 cm/yr, respectively. The width and height of the orogenic wedge increase as the  
 386 convergence rate increases, while keeping the average precipitation constant. At the same time,  
 387 the rock deformation exhibits the tendency from folding toward imbricate thrusting.

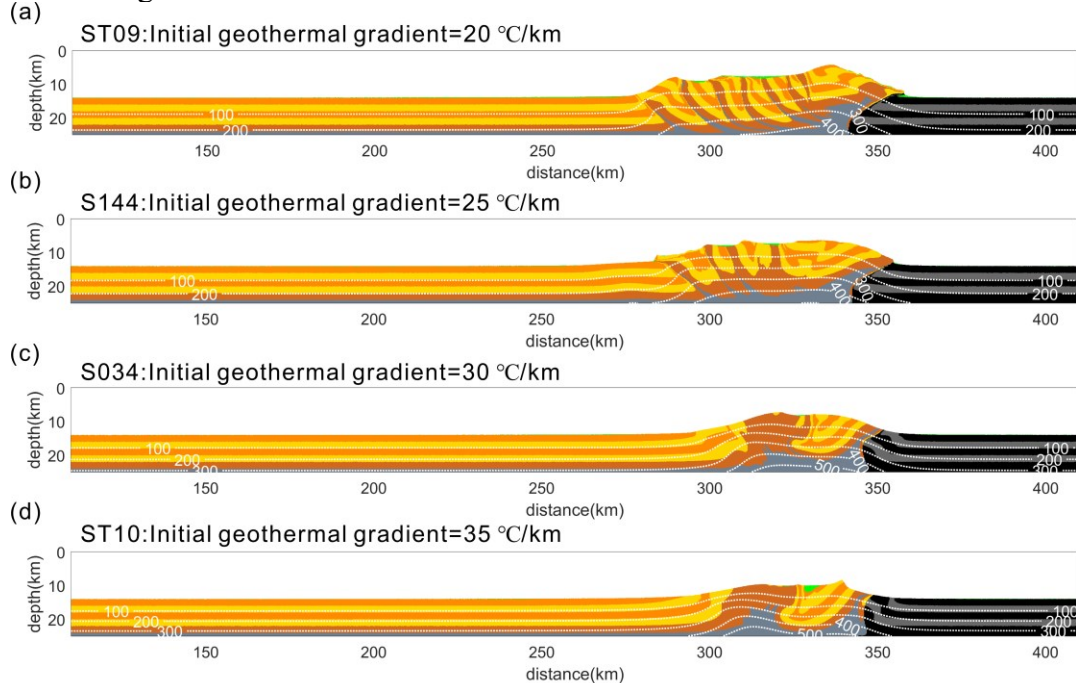
388  
 389 The effect of increasing the average precipitation while fixing the convergence rate is  
 390 opposite to that of increasing the convergence rate while keeping the average precipitation  
 391 constant. When the convergence rate and initial geothermal gradient remain constant, increasing  
 392 the average precipitation favors reducing the height and width of the orogenic wedge (Figure 4).  
 393 At the same time, the deformation style within the orogenic wedge gradually transitions from  
 394 thrusting to folding. Similarly, for models with sufficiently high average precipitation, the  
 395 deformation structures will be quickly eroded, resulting in very low topography (Figure 4d and  
 396 e). These findings suggest that the height, width, and deformation style of a specific orogenic  
 397 wedge primarily rely on the relative strength of tectonic and climatic forces, rather than their  
 398 respective magnitudes. When the tectonic forces are relatively stronger, the orogenic wedge  
 399 tends to broaden, increase in elevation, and develop thrust faults. Conversely, when the tectonic  
 400 forces are relatively weaker, the orogenic wedge tends to narrow, decrease in elevation, and  
 401 develop folds.



402  
 403 **Figure 4.** Numerical modelling results showing the influence of the average precipitation ( $P_0$ ) on  
 404 the evolution of orogenic wedges. The white dashed lines indicate isotherms (in  $^{\circ}\text{C}$ ). For all  
 405 models, the convergence rate ( $v_c$ ) is 2.0 cm/yr, the initial geothermal gradient ( $dT/dh$ ) is  
 406  $30\text{ }^{\circ}\text{C}/\text{km}$ , and the runtime is 8 Myr. The average precipitations for (a), (b), (c), (d) and (e) are 2  
 407 m/yr, 4 m/yr, 6 m/yr, 8 m/yr and 10 m/yr, respectively. The width and height of the orogenic  
 408 wedge decrease as the average precipitation increases, while keeping the convergence rate  
 409 constant. At the same time, the rock deformation exhibits the tendency from imbricate thrusting  
 410 toward folding.

411  
 412 Besides convergence rate and average precipitation, geothermal conditions also play a  
 413 significant role in influencing the evolution of orogenic wedges. Since the geothermal gradients  
 414 at the model's bottom boundary are set to remain consistent with the initial geothermal gradients,  
 415 the initial geothermal gradient not only affects the initial geothermal field but also influences the  
 416 heat flow at the bottom of the model. This means that increasing the initial geothermal gradient  
 417 will enhance the overall geothermal field of the model, and vice versa. Our modelling results  
 418 indicate that, under constant convergence rate and average precipitation, a gentler initial  
 419 geothermal gradient favors developing wider orogenic wedge and higher topography.  
 420 Additionally, it tends to promote the formation of imbricate structures (Figure 5a and b). Models  
 421 with steeper initial geothermal gradients tend to develop narrower orogenic wedges and lower  
 422 topographies, and the deformation style is dominated by folding (Figure 5c and d). In this  
 423 context, increasing the initial geothermal gradient has a comparable effect to strengthening the  
 424 relative dominance of climatic forces over tectonic forces, as both contribute to the softening of  
 425 crustal rocks. This can be attributed to the former enhancing the overall geothermal field, while  
 426 the latter can localize deformation and steepen geothermal gradients. These will elevate the

427 temperature and strain rate of the rocks, leading to a decrease in viscosity, thereby weakening the  
 428 rock strength.



429  
 430 **Figure 5.** Numerical modelling results showing the influence of the initial geothermal  
 431 gradient ( $dT/dh$ ) on the evolution of orogenic wedges. The white dashed lines indicate isotherms  
 432 (in  $^{\circ}\text{C}$ ). For all models, the convergence rate ( $v_c$ ) is 2.0 cm/yr, the average precipitation ( $P_0$ ) is 6  
 433 m/yr, and the runtime is 8 Myr. The initial geothermal gradients for (a), (b), (c) and (d) are  
 434 20  $^{\circ}\text{C}/\text{km}$ , 25  $^{\circ}\text{C}/\text{km}$ , 30  $^{\circ}\text{C}/\text{km}$  and 35  $^{\circ}\text{C}/\text{km}$ , respectively. The width and height of the orogenic  
 435 wedge decrease as the initial geothermal gradient increases. At the same time, the rock  
 436 deformation exhibits the tendency from imbricate thrusting toward folding.

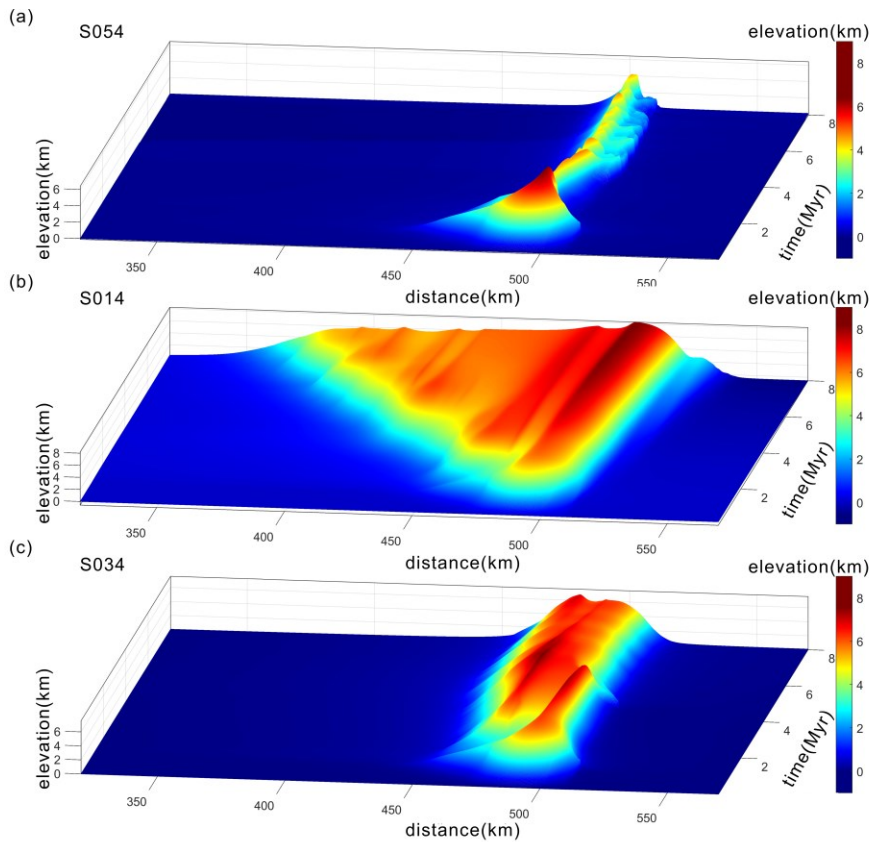
437

#### 438 4.2 Evolutionary regimes of orogenic wedges

439 Based on the relative dominance of tectonic and climatic forces, as well as the features of  
 440 tectonic and topographic evolution, the modelling outcomes can be categorized into three basic  
 441 types of orogenic wedge (or evolutionary regimes), which can be referred as type A, B and C  
 442 (Figure 6). A type A orogenic wedge is dominated by climatic forces compared to tectonic forces  
 443 (Figure 6a). The most typical feature of this type of orogenic wedge is the rapid obliteration of  
 444 initial deformation structures and topography due to intense erosion before reaching a steady  
 445 state. In most cases, this process occurs within approximately 3 Myr, although in a few cases the  
 446 topography may persist for 5~6 Myr. During this phase, there can be rapid and significant  
 447 variations in the structural and topographic characteristics. However, the ultimate tendency is  
 448 towards topographic flattening, resulting in minimal preservation of deformation structures  
 449 (Figure 3a, Figure 4d and e, Figure 5d). Once a steady state is reached, a type A orogenic wedge  
 450 maintains a long-term stable equilibrium of material flux. Conversely, A type B orogenic wedge  
 451 is dominated by tectonic forces compared to climatic forces (Figure 6b). In a type B orogenic  
 452 wedge, the erosional efficiency is insufficient so that the erosional outflux cannot balance the  
 453 tectonic influx. This results in continuous expansion of deformation towards the foreland basin,

454 forming orogenic wedge with large size and high topography. A type B orogenic wedge does not  
 455 attain a stable equilibrium of material flux, and its deformation style is dominated by imbricate  
 456 thrusting.

457



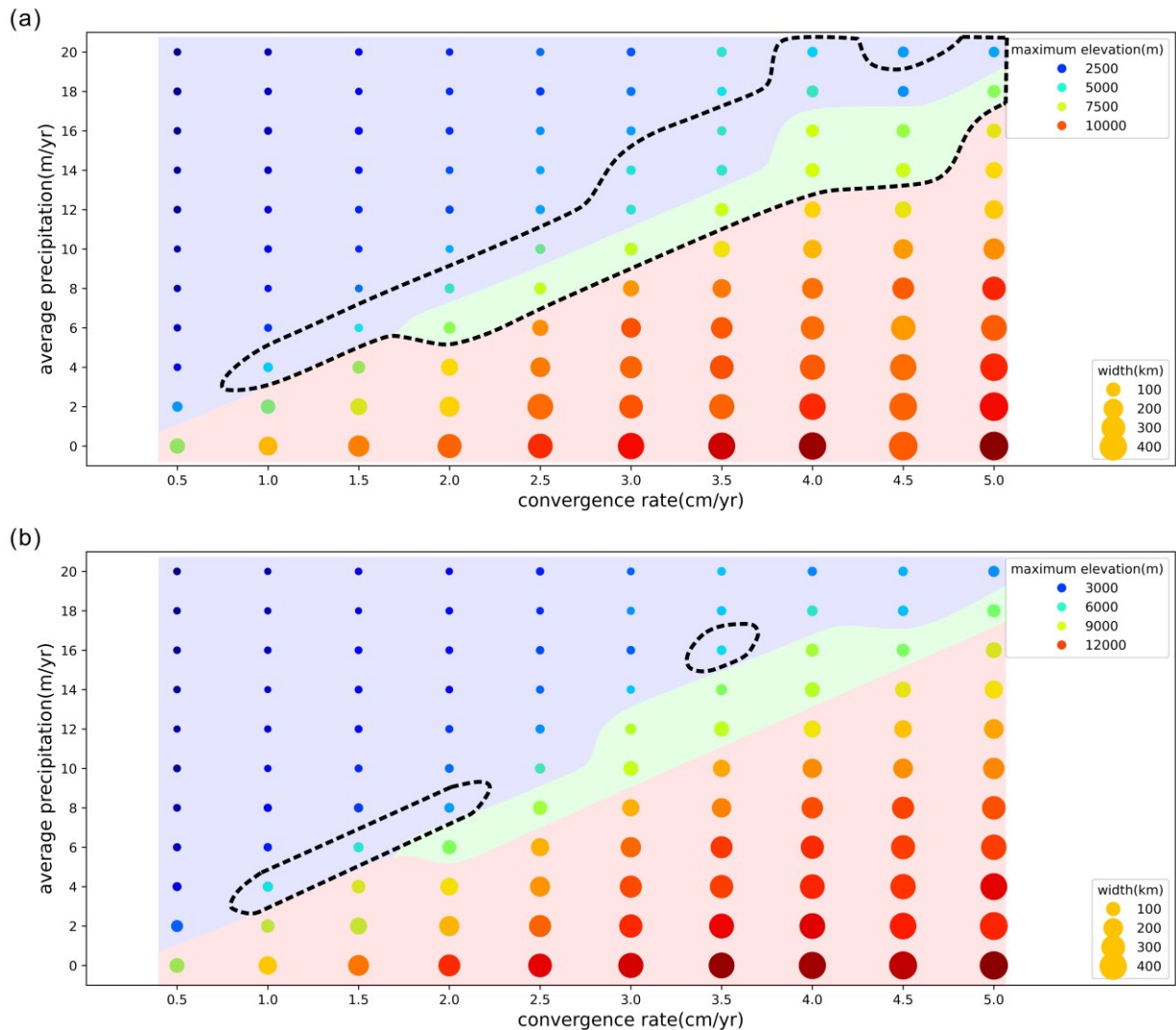
458

459 **Figure 6.** The geomorphic evolution of typical models of three basic types of orogenic wedge.  
 460 (a) is the representative of type A orogenic wedge, which is dominated by the climatic forces. In  
 461 this case, the width and height of the wedge shrink rapidly starting from  $t=1$  Myr until the  
 462 topography is almost entirely erased before reaching a steady state. (b) is the representative of  
 463 type B orogenic wedge, which is dominated by the tectonic forces. In this case, the deformation  
 464 continuously extends towards the foreland basin, leading to high topography and wider wedge.  
 465 (c) is the representative of type C orogenic wedge, in which the climatic and tectonic forces  
 466 exhibit comparable strength. In this case, the material flux reaches a steady state after a brief  
 467 period of adjustment (around 1 Myr). Subsequently, the height, width and the topography of the  
 468 wedge can remain relatively stable in the long-term time.

469

470 When the climatic and tectonic forces exhibit comparable strength, it gives rise to type C  
 471 orogenic wedge (Figure 6c). In this case, the orogenic system is able to establish a dynamic  
 472 equilibrium within a short period of time (around 1 Myr). In this state of equilibrium, the  
 473 material flow field, width of the orogenic wedge, topography and deformation style of rocks can  
 474 remain relatively stable in the long-term time (Figure 3b, Figure 4b, Figure 5b and c). In contrast  
 475 to type A orogenic wedge, a type C orogenic wedge in a state of equilibrium retains a certain  
 476 amount of deformation structures, resulting in a relatively larger size. The deformation style in a

477 type C orogenic wedge is variable and it can manifest as either imbricate thrusting (Figure 5b) or  
 478 folding (Figure 5c), depending on the shallow crustal geothermal field or other factors.  
 479



480  
 481 **Figure 7.** Orogenic wedge type as a function of convergence rate and average precipitation for  
 482 cases with an initial geothermal gradient of 30 (a) and 25 (b) °C/km. Each point inside the  
 483 diagrams represents one numerical experiment in Table S2 and S3 in Supporting Information S1.  
 484 The color and size of each point indicate the maximum elevation and width of the orogenic  
 485 wedge (at  $t=8$  Myr), respectively. The regions marked in light blue, light red, and light green  
 486 correspond to the orogenic wedges categorized as type A, B and C, respectively. Enclosed within  
 487 the dashed circle are the models that exhibit similar structural features to the eastern Himalayan  
 488 syntaxis (Type D zone). The distribution of type A, B and C orogenic wedges doesn't show  
 489 significant variation when the initial geothermal gradient changes, but the Type D zone shrinks  
 490 as the initial geothermal gradient decreases.

491

492 In the parameter space of the average precipitation and convergence rate, a certain  
 493 regularity can be observed about the distribution of the three basic types of orogenic wedges  
 494 (Figure 7). Irrespective of whether the initial geothermal gradient is 30 or 25 °C/km, type C

495 orogenic wedges are primarily located near the line  $P_0 = 4 \times v_c - 2$  (where  $P_0$  is in units of  
 496 m/yr,  $v_c$  is in units of cm/yr, and  $v_c > 1.5$  cm/yr), while type A and type B orogenic wedges are  
 497 distributed above and below this line, respectively. This distribution pattern remains relatively  
 498 stable regardless of the variation in the initial geothermal gradient. This is reasonable because the  
 499 three basic types of orogenic wedges are essentially the result of different relative strengths of  
 500 tectonic and climatic forces, and this distribution pattern corresponds to different parameter  
 501 ranges of different relative strengths between the two forces.  
 502



503  
 504 **Figure 8.** Typical models that exhibit similar structural features to the eastern Himalayan  
 505 syntaxis. The white dashed lines indicate isotherms (in °C). When the convergence rate, average  
 506 precipitation and initial geothermal gradient fall within certain ranges, several significant  
 507 structural features resembling those observed in the syntaxis will emerge within the orogenic  
 508 wedge. At a particular geological time ( $t$ ) during model evolution, sustained, stationary, and  
 509 localized erosion induces localized rock uplift and deformation, forming large-scale antiforms. In  
 510 the core areas of the antiforms, extreme relief, deep exhumation, intense deformation and  
 511 steepening of the near-surface thermal gradient overlap spatially.  
 512

513 Among type A and type C orogenic wedges, we identified a fourth special type of  
 514 orogenic wedge (referred as type D), which exhibits similar structural features to the eastern

515 Himalayan syntaxis at a particular geological time (Figure 8). When the convergence rate,  
 516 average precipitation and initial geothermal gradient fall within certain ranges, it leads to the  
 517 development of sustained, stationary, and localized erosion within the orogenic wedge. This  
 518 further induces rapid uplift of rocks in a local area, forming large-scale antiforms. In the core  
 519 areas of the antiforms, extreme relief, deep exhumation, intense deformation and steepening of  
 520 the near-surface thermal gradient overlap spatially. These structural features closely approximate  
 521 the field observations in the eastern Himalayan syntaxis region. However, for those orogenic  
 522 wedges that belong to both type D and type A, such antiformal structures cannot be preserved for  
 523 a very long time. Generally, they are completely destroyed within around 1 Myr after their  
 524 formation, but for those belonging to both type D and type C, these structures can be sustained  
 525 for a longer period (usually >2 Myr). Similar to type C orogenic wedges, the majority of the type  
 526 D orogenic wedges conform to the condition of relatively balanced climatic and tectonic forces,  
 527 but their distributions in the  $P_0 - v_c$  parameter space do not align perfectly (Figure 7). Here we  
 528 refer to the domain corresponding to type D orogenic wedges in the  $P_0 - v_c$  parameter space as  
 529 “Type D zone”. Unlike the distribution pattern of the three basic types, the Type D zone is highly  
 530 sensitive to the initial geothermal gradient, and it shrinks considerably when the initial  
 531 geothermal gradient decreases from 30 to 25 °C/km. Moreover, it can be observed that the Type  
 532 D zone tends to expand with an increase in the initial geothermal gradient or average  
 533 precipitation increase (Figure 7). As discussed above, the increase in initial geothermal gradient  
 534 and average precipitation promotes a decrease in effective viscosity of crustal rocks. This  
 535 finding implies that the softening of the crustal rocks appears to favor the formation of  
 536 syntaxes.

537 Our results indicate that the tectonic and topographic evolution of an orogenic wedge is  
 538 the result of the combined effects of crustal shortening, precipitation, and geothermal field.

## 539 **5 Discussion**

### 540 **5.1 Model limitations**

541 The distribution pattern depicted in Figure 7 is related to the initial model configuration. It  
 542 can be inferred that the distribution of different types of orogenic wedges in  $P_0 - v_c$  parameter  
 543 space may vary slightly if the initial model configuration, such as the rheology of the initial  
 544 undeformed rock sequence, is altered. Therefore, it may not perfectly fit every similar numerical  
 545 model or orogenic region. Nevertheless, the regularities revealed by regime diagram (Figure 7)  
 546 are expected to exist in nature. Moreover, although the type D orogenic wedges closely match  
 547 the field observations from the eastern Himalayan syntaxis in various aspects, some crucial  
 548 features still haven’t been reproduced in our simulation. For instance, although a simple partial  
 549 melting model is included in our simulation, obvious partial melting of rocks is not observed in  
 550 the type D orogenic wedges. Nevertheless, the depression melting process in the eastern  
 551 Himalayan syntaxis since 10 Ma is widely recognized (Booth et al., 2009; Koons et al.,  
 552 2013). This discrepancy is probably attributed to the simplifications in our initial model  
 553 configuration, including simplified profile of rock sequence and thermal structure. The initial  
 554 state of the eastern Himalayan syntaxis around 8 million years ago was more complex than we  
 555 assumed.

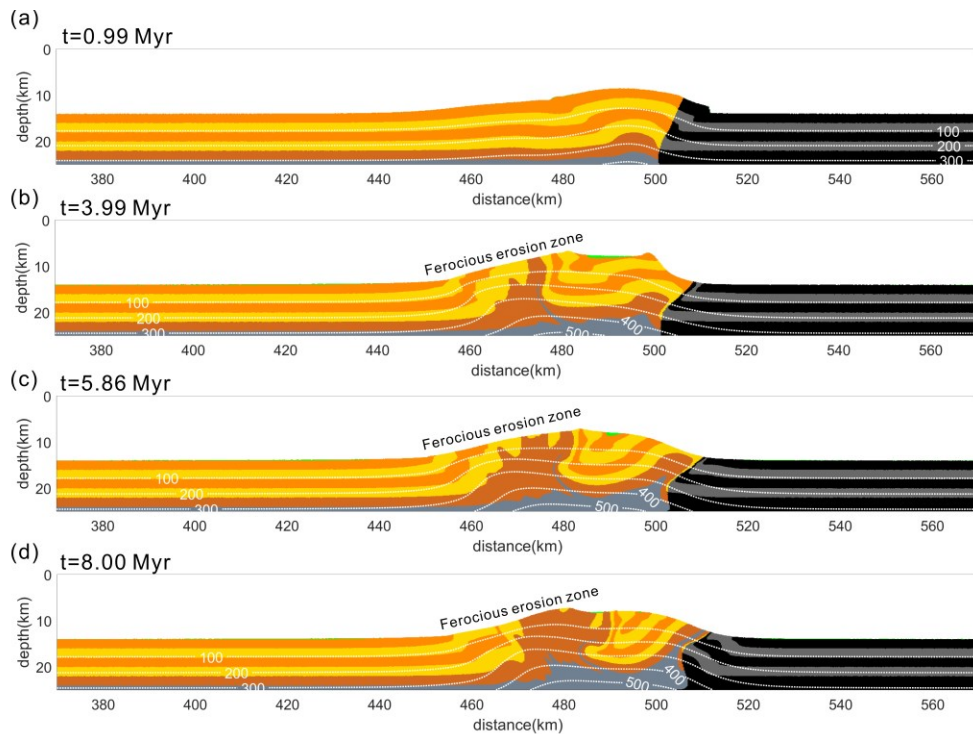
556 For simplicity, we assume that the surface processes are fluvially-dominated. In other words,  
 557 above the ELA, we substitute fluvial erosion for glacial erosion. This will inevitably introduce  
 558 errors. Most of our modelling results, especially the type B orogenic wedges, exhibit peak

559 elevations far exceeding the highest peak on Earth (8848 m) (Figure 7). This could be due to the  
 560 absence of an accurate glacial erosion process in our models. Glaciers can limit mountain height  
 561 through a distinct mechanism of erosion, known as glacial buzzsaw (Egholm et al., 2009).  
 562 Therefore, coupled surface process model accounting for both fluvial and glacial activities is  
 563 necessary for more accurate modelling of landscape evolution in the eastern Himalayan syntaxis  
 564 region.

565 In order to simulate the co-evolution of topography and climate, we employed a simplified  
 566 model for orographic precipitation (Equation 9). While this precipitation model can capture the  
 567 primary characteristics of precipitation distribution in mountainous regions, it tends to  
 568 overestimate the precipitation in the inland areas on the leeward side of the mountain ranges and  
 569 leads to minor unrealistic erosion (Text S3 and Figure S1 in Supporting Information S1, Figure 9  
 570 and 10). In the future, constructing more realistic precipitation models could be a promising  
 571 research direction.

572 Since orogenic wedges or syntaxes are three-dimensional in reality, the 2D geometry  
 573 employed in this study renders the models inadequate for addressing a number of significant  
 574 aspects of orogenic development, such as the growth of structures oriented parallel to plate  
 575 boundaries, the development of possible strike-slip faults and the evolution of 2D topography,  
 576 etc. Therefore, this work would be greatly improved if these geological processes are simulated  
 577 in 3D models.

578

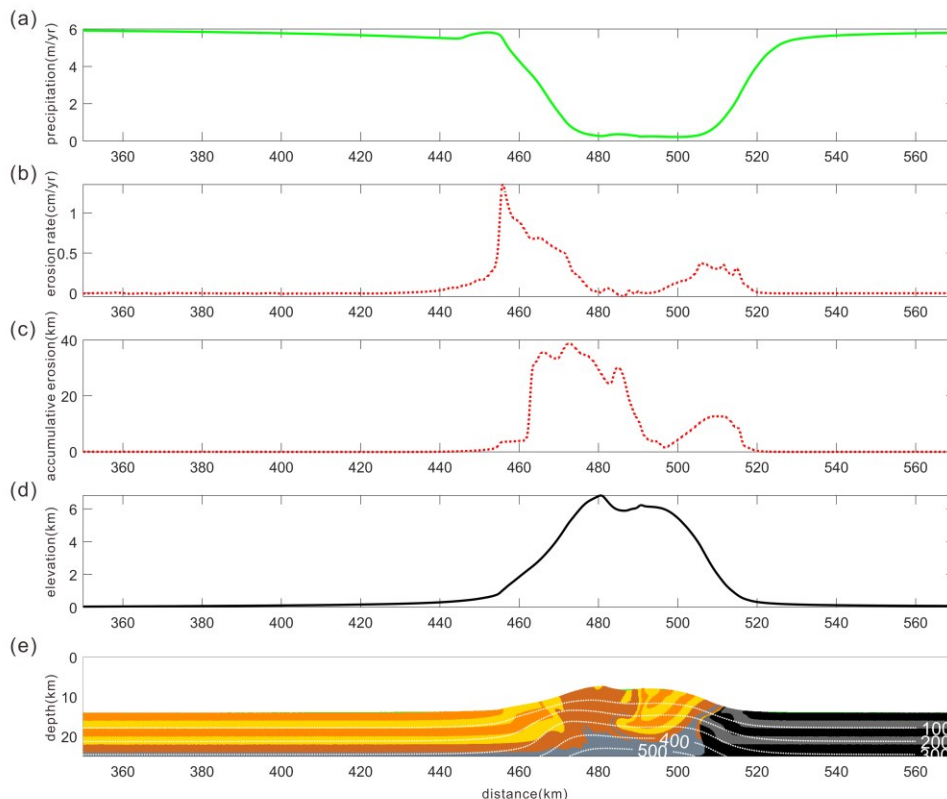


579

580 **Figure 9.** Modelling results showing the evolution of model S034. The white dashed lines  
 581 indicate isotherms (in °C). The orographic precipitation applied from  $t=1$  Myr induces rapid  
 582 erosion within a narrow zone on the windward flank. Most of the material entering the orogenic  
 583 wedge “flows out” through this narrow window, resulting in relatively stable positioning of the  
 584 zone with rapid erosion and the width of the orogenic wedge. Sustained, stationary, localized and  
 585 rapid erosion induces rapid uplift of rocks in local area, leading to the formation of a large-scale  
 586 antiform.

## 587 5.2 Comparison with the eastern Himalayan syntaxis

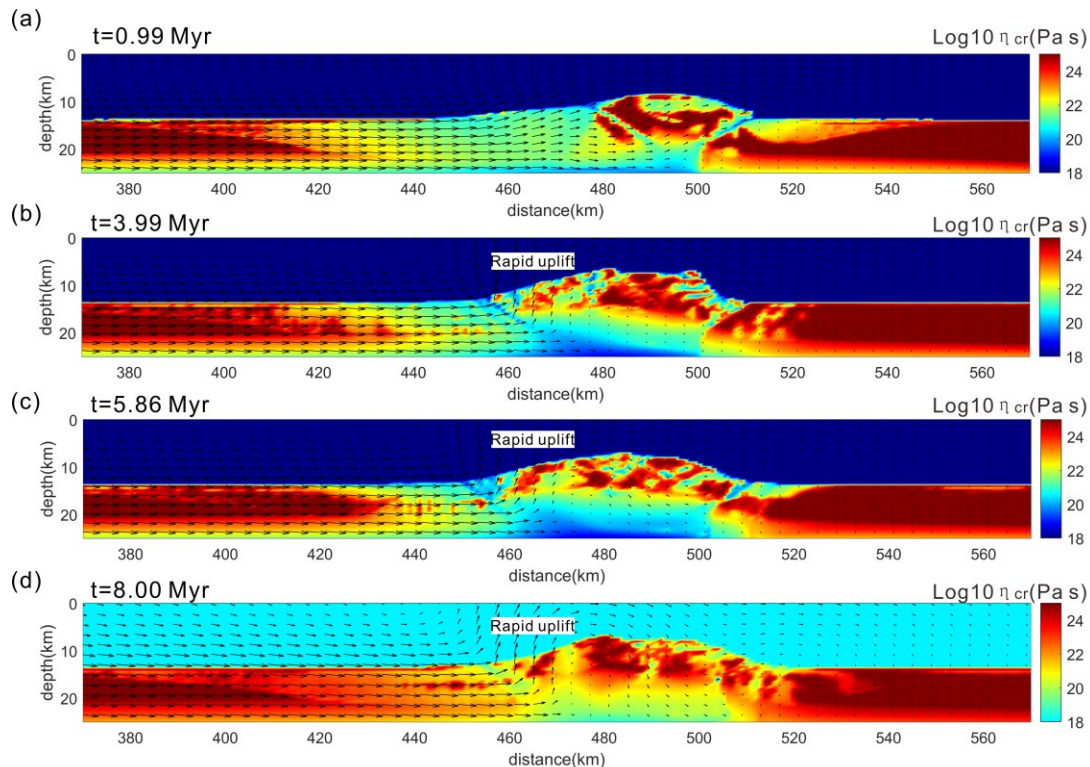
588 Taking account of parameter selection and modelling results, we identify that model S034  
 589 best matches the field observations from the eastern Himalayan syntaxis (Figure 9 and 10). In  
 590 model S034, the applied orographic precipitation starting at  $t=1$  Myr induces rapid erosion within  
 591 a narrow zone (20~25 km scale) on the windward flank of the orogenic wedge (Figure 9 and  
 592 10b). Rapid erosion and decompression further result in rapid uplift, exhumation, and  
 593 deformation of local rocks (Figure 9 and 11). It can be observed that the position of this intense  
 594 erosion zone and the width of the orogenic wedge remain relatively stable in the long-term time  
 595 (several million years), indicating a relative equilibrium in the material influx and outflux. This  
 596 implies that most of the material entering the orogenic wedge “flows out” of this limited area via  
 597 the narrow erosional window. The magnitudes of the crucial parameters (such as convergence  
 598 rate, average precipitation and initial geothermal gradient) and the underlying physics  
 599 (conservation of mass, momentum and energy, rheology, orographic precipitation, surface  
 600 processes, etc.) ensure that the model develops sustained, stationary, localized, rapid erosion, and  
 601 decompression on the windward flank. This further induces sustained, rapid rock uplift,  
 602 exhumation, and deformation in the local area, ultimately forming a large-scale antiform (Figure  
 603 9 and 10). These outcomes appear to be the inevitable results of the delicate equilibrium among  
 604 tectonic forces, climatic forces and crustal thermal structure under various physical laws.  
 605



606 **Figure 10.** Modelling results of model S034 at  $t=8$  Myr. The modelling results closely  
 607 approximate various significant aspects of the field observations from the eastern Himalayan  
 608 syntaxis. (a), (b), (c) and (d) represent the precipitation, transient erosion rate, accumulative  
 609 erosion and topography along the model cross-section profile, respectively. (e) demonstrates the  
 610 deformation pattern of the model, where white dashed lines indicate isotherms (in  $^{\circ}\text{C}$ ).  
 611

612 In model S034, the spatial scale of the area with rapid exhumation and intense  
 613 deformation in the core of the antiform is about 25 km, which is close to the actual observations  
 614 from the eastern Himalayan syntaxis (Koons et al., 2013; Zeitler, Meltzer, et al., 2001). The  
 615 transient erosion rate of 0.5~1.4 cm/yr within the intense erosion zone (Figure 10b) also matches  
 616 the decadal erosion rate reported by Enkelmann et al. (2011) based on the study of detrital  
 617 zircon. The accumulative erosion (20~40 km) within this zone is slightly greater than the  
 618 exhumation (>20 km) inferred from P-T estimates and thermochronological dating (Figure 10c)  
 619 (Koons et al., 2013). This is reasonable because the rock trajectories within the orogenic wedge  
 620 are usually non-vertical. Furthermore, the maximum elevation in the core of the antiform reaches  
 621 approximately 6817 m, which is comparable to the elevations of the two main peaks, Namche  
 622 Barwa Peak (7782 m) and Gyala Peri Peak (7294 m), in the eastern Himalayan syntaxis region.

623



624

625 **Figure 11.** The evolution of the viscosity and velocity field in model S034. Within the intense  
 626 erosion zone on the windward flank of the orogenic wedge, rapid erosion and decompression  
 627 induce continuous and rapid uplift of rocks. However, the model doesn't show a significant  
 628 decrease in the viscosity of rocks within this intense erosion zone.

629

630 However, the selected average precipitation of 6 m/year in model S034 is much higher  
 631 than the current average precipitation (~2 m/yr) in the eastern Himalayan syntaxis region  
 632 (Anders et al., 2006; Bookhagen & Burbank, 2006), although this value may not align well with  
 633 the historical precipitations. It's important to note that, due to the model limitations, the erosion  
 634 rates generated by our surface processes model may be underestimated for two reasons. Firstly,  
 635 the glacial erosion was not fully accounted for in our model. Secondly, our modelling on  
 636 landscape evolution employs a 3-by-N grid, which may result in lower water discharge at each  
 637 point compared to real-world conditions, leading to lower erosion rates. Therefore, to achieve a  
 638 better approximation of the actual erosional efficiency in the eastern Himalayan syntaxis region,

639 a higher average precipitation would be required. In addition, the convergence rate of 2.0 cm/yr  
 640 in model S034 is consistent with the Himalayan shortening rate obtained from the reconstruction  
 641 of the India-Asia convergence history (Guillot et al., 2003). A relatively steep initial geothermal  
 642 gradient of 30 °C/km also approximates the relatively hot regime that characterized the majority  
 643 of the Himalayan-Tibetan Plateau soon after the collision (Zhang et al., 2022).

644 In summary, the simulation results of model S034 closely match the field observations in  
 645 the eastern Himalayan syntaxis region from various perspectives, indicating that our modelling  
 646 scheme is applicable to the study area. Therefore, the mechanisms of tectonic and geomorphic  
 647 evolution revealed by the model are reliable.

### 648 5.3 Syntaxis as the result of the combined effects of multiple factors

649 Our modelling results indicate that different combinations of tectonic and climatic forces  
 650 result in various types of orogenic wedges. The three basic types of orogenic wedge mentioned  
 651 above closely resemble the three end-member types of growing orogens proposed by Wolf et al.  
 652 (2022). The only difference is that their model is defined on a larger scale (mantle-scale), while  
 653 our model operates at a relatively smaller scale, specifically limited to the orogenic wedges or  
 654 fold and thrust belts. Wolf et al. (2022)'s modelling study also shows that the topographic  
 655 evolution of collisional orogens is determined by the combination of plate velocity, crustal  
 656 rheology and surface process efficiency. As early as the end of the last century, Avouac and  
 657 Burov (1996) had proposed that there is a coupled regime allowing for mountain growth. They  
 658 showed that mountain growth only occurs when the surface mass diffusion and lithospheric  
 659 shortening exhibit comparable efficiency, otherwise the mountain will “collapse”. Similar  
 660 combined effect of tectonic and climatic forces was also identified in smaller-scale models  
 661 (Simpson, 2004). This is also supported by the analytical treatment studies. For instance, Roe et  
 662 al. (2006) have found that the width ( $L$ ) or height ( $R_c$ ) of a fluvial-dominated steady-state  
 663 orogenic wedge is related to both accretionary flux ( $F$ ) and average precipitation ( $P_0$ ):

$$664 R_c(\text{or } L) \propto F^{\frac{1}{1+h_k m}} P_0^{\frac{-m}{1+h_k m}} \quad (11)$$

665 where  $m$  and  $n$  are the discharge and slope exponents, respectively (Whipple & Tucker, 1999).  
 666  $h_k$  is the Hack's law exponent (Hack, 1957).

667 Considering the initial thickness of the incoming plate ( $H$ ) to be relatively constant for a  
 668 specific orogenic wedge, the accretionary flux can be rewritten as (Dahlen, 1990; Whipple &  
 669 Meade, 2004):

$$670 F = H v_c \quad (12)$$

671 where  $v_c$  is the convergence rate. Substituting Equation (12) into Equation (11) and rearranging:

$$672 R_c(\text{or } L) \propto \left( \frac{P_0^m}{v_c} \right)^{\frac{-1}{1+h_k m}} H^{\frac{1}{1+h_k m}} \quad (13)$$

673 since  $H$  is assumed to be relatively constant, we get:

$$674 R_c(\text{or } L) \propto \left( \frac{P_0^m}{v_c} \right)^{\frac{-1}{1+h_k m}} \quad (14)$$

675 From the perspective of energy, the convergence rate and average precipitation can be  
 676 regarded as significant indicators of the strength of tectonic and climatic forces, respectively

677 (Xiangjiang & Dalai, 2017). As shown by our modelling results, Equation (14) supports the  
 678 perspective that the height and width of a specific orogenic wedge primarily rely on the relative  
 679 strength of tectonic and climatic forces, rather than their respective magnitudes. As  $m$  and  $h_k$   
 680 are typically positive (Montgomery & Dietrich, 1992; Whipple & Tucker, 1999), Equation (14)  
 681 suggests that the height and width of an orogenic wedge decrease with increasing ratio of  
 682 average precipitation to convergence rate, which is consistent with our modelling results (Figures  
 683 3, 4 and 7). The proportionality symbol ( $\propto$ ) in Equation (14) implies that there are other factors  
 684 influencing the evolution of orogenic wedges, such as rock erodibility, orogen geometry, and  
 685 critical taper angle (Roe et al., 2006; Roe et al., 2008). According to our modelling, the  
 686 geothermal gradients within the crust is also one of the important factors.

687 Here we assume that the maximum elevation of an orogenic wedge ( $MaxE$ ) is  
 688 proportional to its height. Then, based on Equation (14), if the convergence rate holds constant,  
 689 we have:

$$MaxE \propto P_0^{x_1} \quad (15)$$

690 or

$$MaxE = A_1 P_0^{x_1} \quad (16)$$

692 In the same way, if the average precipitation holds constant, we have:

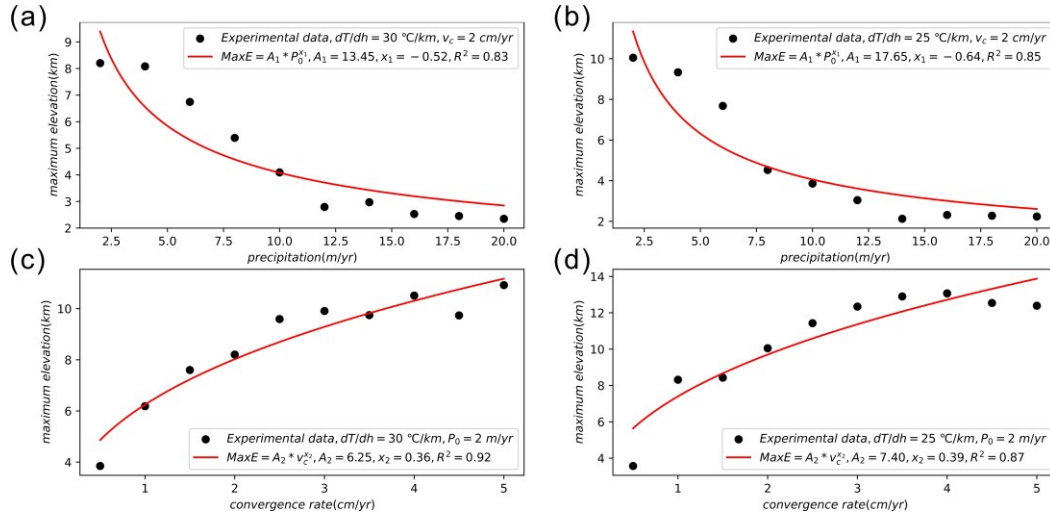
$$MaxE \propto v_c^{x_2} \quad (17)$$

693 or

$$MaxE = A_2 v_c^{x_2} \quad (18)$$

694 where  $A_1, A_2, x_1, x_2$  are coefficients.

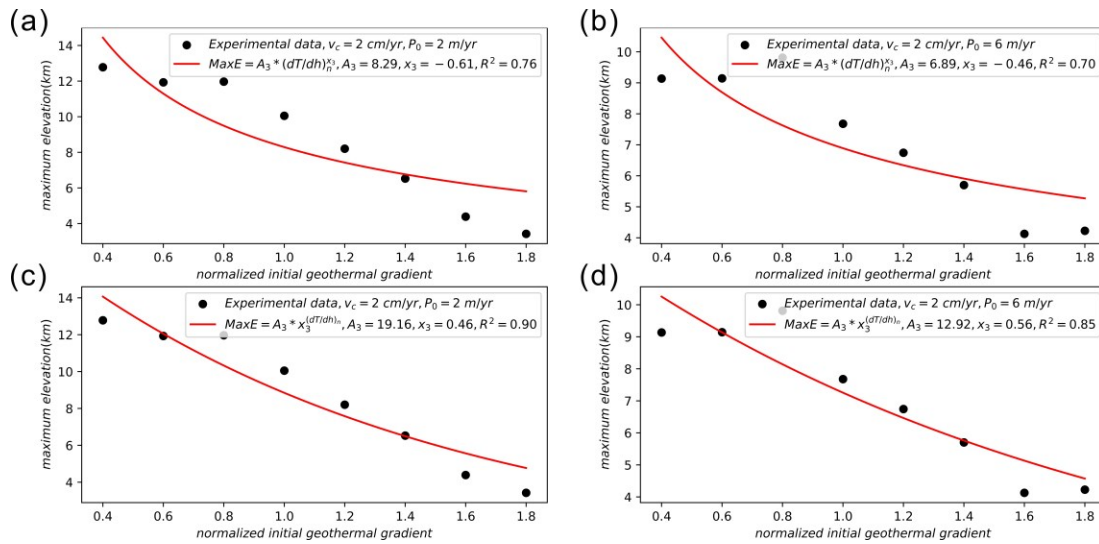
698



699 **Figure 12.** The relationships between the maximum elevations of orogenic wedges and the  
 700 average precipitations ((a) and (b)) or convergence rates((c) and (d)). Each black dot represents  
 701 one numerical experiment. Experiments in (a) and (b) have a convergence rate of 2 cm/yr and  
 702 initial geothermal gradients of 30 °C/km and 25 °C/km, respectively, while experiments in (c)  
 703 and (d) have an average precipitation of 2 m/yr and initial geothermal gradients of 30 °C/km and  
 704 25 °C/km, respectively. The red solid lines represent the best-fit curves obtained through least-  
 705 squares method using Equation (16) for (a) and (b), and Equation (18) for (c) and (d). The fitting  
 706 results ( $R^2 > 0.83$ ) indicate a good power-law relationship between the maximum elevations of  
 707 orogenic wedges and both the average precipitations and convergence rates.

708

710 To further confirm the above relationships, we performed a least-squares fitting on our  
 711 experimental data (Figure 12). In Figure 12a and b, the black dots represent the experiments with  
 712 a convergence rate of 2 cm/yr and initial geothermal gradients of 30 °C/km and 25 °C/km,  
 713 respectively. Equation (16) was used for fitting, and the fitted values of  $x_1$  are -0.52 and -0.64,  
 714 with corresponding  $R^2$  of 0.83 and 0.85. Similarly, in Figure 12c and d, the experiments have an  
 715 average precipitation of 2 m/yr and initial geothermal gradients of 30 °C/km and 25 °C/km,  
 716 respectively. Equation (18) was used for fitting, and the fitted values of  $x_2$  are 0.36 and 0.39,  
 717 with corresponding  $R^2$  of 0.92 and 0.87. Theoretically, the values of  $x_1$  and  $x_2$  should be -0.25  
 718 and 0.5, respectively (assuming  $m = 0.5$  and  $h_k = 2$  as suggested by Whipple and Tucker  
 719 (1999) and Montgomery and Dietrich (1992)). The deviation between the theoretical and fitted  
 720 values may attribute to the more complex precipitation, surface processes and rheology  
 721 considered in our model. Nevertheless, both analytical treatment and our numerical modelling  
 722 indicate that there is a specific power-law relationship between the orogen height and the average  
 723 precipitation or convergence rate, with negative and positive exponents for average precipitation  
 724 and convergence rate, respectively.  
 725



726 **Figure 13.** The relationships between the maximum elevations of orogenic wedges and initial  
 727 geothermal gradients. Each black dot represents one numerical experiment. Experiments in (a)  
 728 and (c) have a convergence rate and average precipitation of 2 cm/yr and 2 m/yr, respectively,  
 729 while experiments in (b) and (d) have a convergence rate of 2 cm/yr and an average precipitation  
 730 of 6 m/yr. The red solid lines represent the best-fit curves obtained through least-squares method  
 731 using Equation (20) for (a) and (b), and Equation (21) for (b) and (d). The fitting results indicate  
 732 that the exponential equation provides a better fit than the power-law equation, suggesting a  
 733 higher probability of an exponential relationship between the maximum elevation of an orogenic  
 734 wedge and the initial geothermal gradient.  
 735

736  
 737 According to our modelling results (Figure 5), it is conceivable that the relationship  
 738 between the maximum elevation of an orogenic wedge and the initial temperature gradient may  
 739 follow a similar pattern as its relationship with the average precipitation. In other words, under  
 740 the condition of constant convergence rate and average precipitation, we may have:

$$MaxE \propto (dT/dh)_n^{x_3} \quad (19)$$

741 or

743 
$$MaxE = A_3(dT/dh)_n^{x_3} \quad (20)$$

744 where  $A_3$  and  $x_3$  are coefficients.  $(dT/dh)_n$  is the initial temperature gradient normalized by  
 745 average shallow crustal geothermal gradient (25 °C/km). However, when Equation (20) is used  
 746 for fitting, the resultant goodness of fit is not satisfactory (Figure 13a and b). For two sets of  
 747 experimental data with a convergence rate of 2 cm/yr and average precipitation of 2 m/yr and 6  
 748 m/yr, respectively, the corresponding  $R^2$  are 0.76 and 0.70. This suggests that the relationship  
 749 between the maximum elevation and the initial temperature gradient may not follow a power-law  
 750 relationship. On the contrary, it is more likely to exhibit an exponential function relationship:

751 
$$MaxE = A_3 x_3^{(dT/dh)_n} \quad (21)$$

752 When fitting the same dataset using Equation (21), we achieved significantly improved  
 753 goodness of fit (the fitted values of  $x_3$  are 0.46 and 0.56, with corresponding  $R^2$  of 0.90 and  
 754 0.85, as depicted in Figure 13c and d). This indicates that Equation (21) is more likely to reveal  
 755 the quantitative relationship between the maximum elevation and the initial temperature gradient  
 756 compared to Equation (20).

757 Combining Equations (15), (17) and (21) gives:

758 
$$MaxE \propto P_0^{x_1} v_c^{x_2} x_3^{(dT/dh)_n} \quad (22)$$

759 or

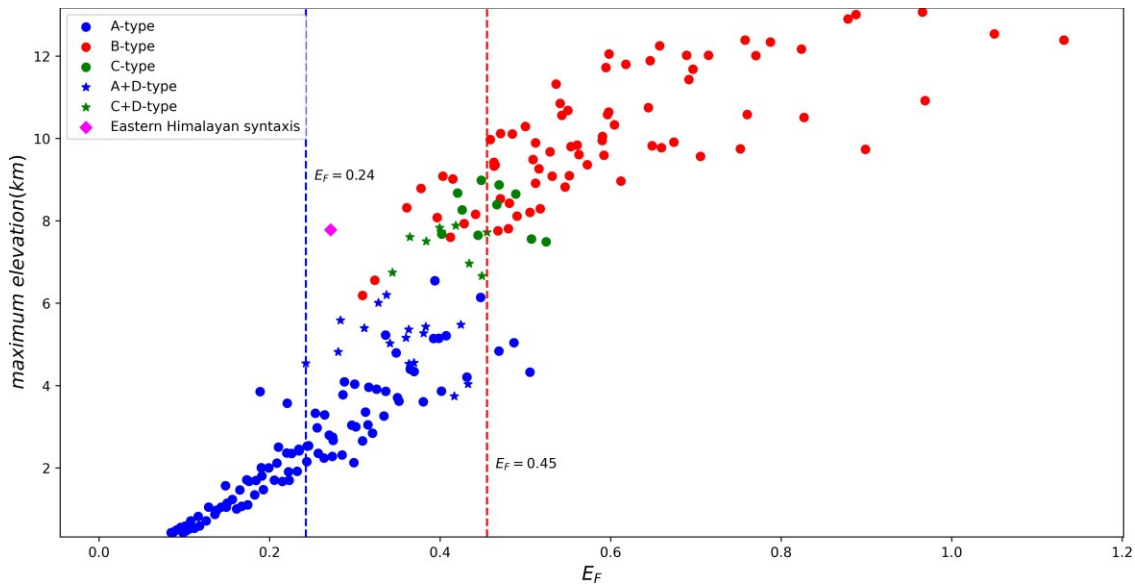
760 
$$MaxE = A * P_0^{x_1} v_c^{x_2} x_3^{(dT/dh)_n} \quad (23)$$

761 similarly,  $A$ ,  $x_1$ ,  $x_2$  and  $x_3$  are coefficients. To unveil the combined effect of average  
 762 precipitation, convergence rate, and initial temperature gradient on the topographic evolution, we  
 763 conducted a least-squares fitting on the data from 212 experiments in this study (excluding the  
 764 20 experiments with zero precipitation) using Equation (23). The fitted values of  $x_1 = -0.35$ ,  
 765  $x_2 = 0.71$  and  $x_3 = 0.46$  were obtained, with a corresponding  $R^2$  of 0.82. The fitted values of  
 766  $x_1$ ,  $x_2$  and  $x_3$  are sensitive to the dataset used. Statistical analysis of the above fitted values  
 767 obtained from different datasets showed that the population standard deviations of the fitted  
 768 values of  $x_1$ ,  $x_2$  and  $x_3$  are 0.12, 0.16, and 0.047, respectively, none of which exceeds 33% of the  
 769 absolute value of the mean of the fitted values, indicating that the coefficients are relatively  
 770 stable. Based on Equation (23), we define the following parameter ( $E_F$ ):

771 
$$E_F = P_0^{-0.35} v_c^{0.71} 0.46^{(dT/dh)_n} \quad (24)$$

772 This parameter can be used to evaluate the combined effect of average precipitation,  
 773 convergence rate and crustal thermal structure on the topographic evolution of an orogenic  
 774 wedge. As shown in Figure 14, on the whole, the maximum elevation of the orogenic wedge  
 775 increases with an increase in  $E_F$ . However, when  $E_F > 0.45$ , the slope becomes gentler, indicating  
 776 that the orogenic wedge may be in a critical state around  $E_F \approx 0.45$ . On either side of this  
 777 critical state ( $E_F < 0.45$  or  $E_F > 0.45$ ), the evolution of an orogenic wedge seems to exhibit different  
 778 patterns. This suggests that orogen is not simply a linear system (Phillips et al., 2003), and highly  
 779 complex nonlinear mechanisms may be involved during its evolutionary process. Moreover, it is  
 780 evident that most of the type A and B orogenic wedges are distributed on the left and right sides  
 781 of line  $E_F = 0.45$ , respectively, while type C orogenic wedges are distributed around this line.  
 782 Type D orogenic wedges are primarily concentrated within the narrow band of  $0.24 < E_F < 0.45$ .  
 783 Admittedly, the four types of orogenic wedges cannot be perfectly identified through the value of  
 784  $E_F$ . This may be attributed to the fact that most experiments at the boundaries of two different  
 785 types of orogenic wedges in Figure 7 are actually transitional types, and they were assigned to  
 786 the category that best represents their most prominent features. This is inevitable and it may have  
 787 introduced some degree of error. Nevertheless, our modelling results indicate that the tectonic

788 and geomorphic evolution of the orogenic wedge is closely related to parameter  $E_F$ . Furthermore,  
 789 we estimated the  $E_F$  of the eastern Himalayan syntaxis based on a convergence rate of 2.0 cm/yr  
 790 (Guillot et al., 2003), an average precipitation of 2.0 m/yr (Anders et al., 2006; Bookhagen &  
 791 Burbank, 2006) and a crustal geothermal gradient of 50 °C/km (Craw et al., 2005). The result  
 792 shows that the  $E_F$  (0.27) of the eastern Himalayan syntaxis is also situated within the specific  
 793 range, implying that the tectonic and geomorphic evolution of the syntaxis is not solely  
 794 influenced by a single factor but the result of the combined effects of multiple factors (Figure  
 795 14).  
 796

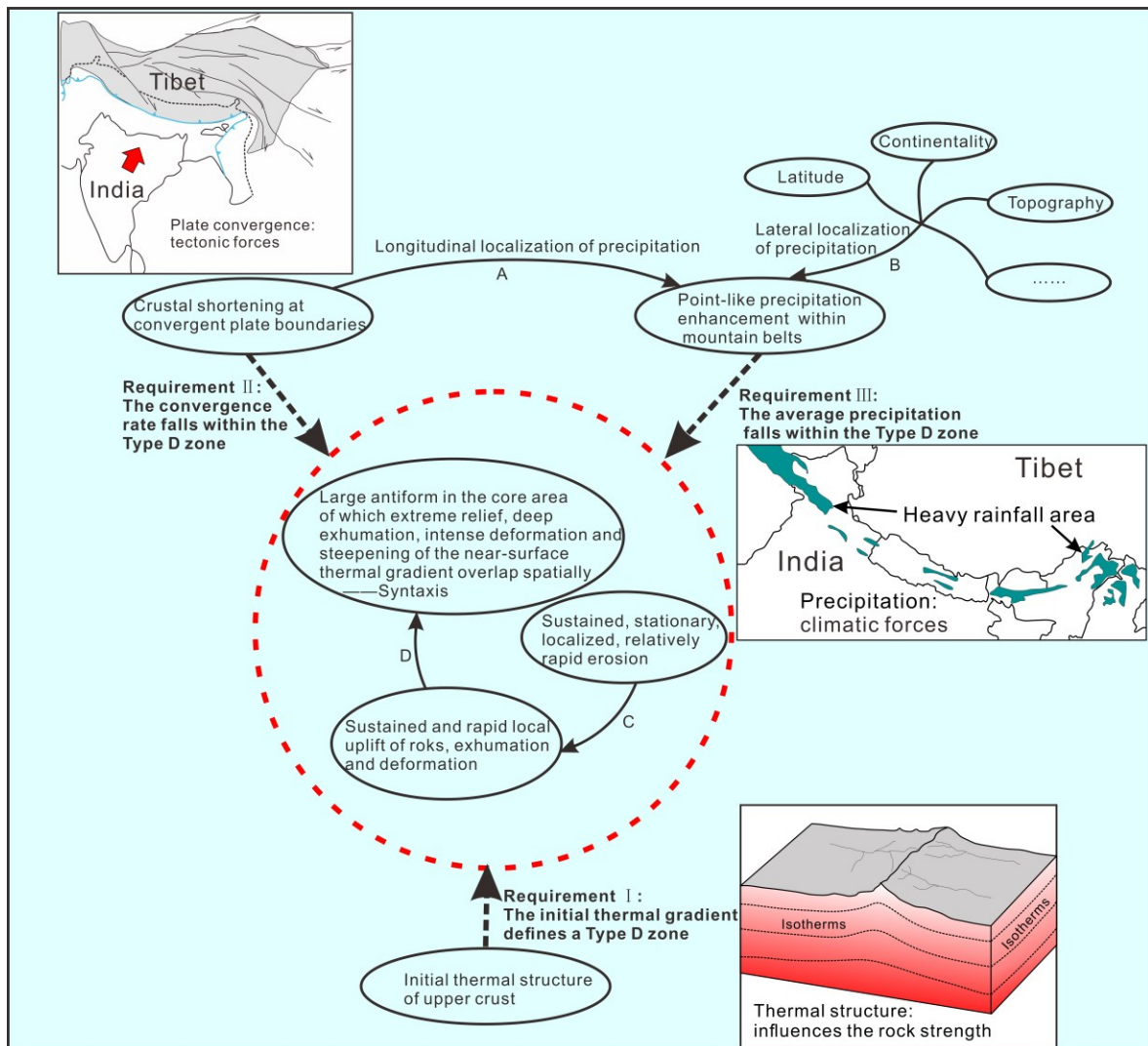


797  
 798 **Figure 14.** Plot of the maximum elevation of the orogenic wedges against  $E_F$ . The dots and stars  
 799 represent the 200 experiments from Table S2 and S3 in Supporting Information S1 (20  
 800 experiments with average precipitation of 0 m/yr are excluded). The blue, red and green colors  
 801 correspond to type A, B and C orogenic wedges, respectively. The stars represent orogenic  
 802 wedges that exhibit similar structural features to the eastern Himalayan syntaxis (type D). Most  
 803 of the type A and B orogenic wedges are distributed on the left and right sides of line  $E_F = 0.45$ ,  
 804 respectively, while type C orogenic wedges are distributed around this line. Type D orogenic  
 805 wedges are primarily concentrated within the narrow band of  $0.24 < E_F < 0.45$ , and the eastern  
 806 Himalayan syntaxis, depicted as a fuchsia diamond, is also situated within this specific range. On  
 807 the whole, the maximum elevation of orogenic wedges is proportional to  $E_F$ , but the slope  
 808 becomes gentler when  $E_F > 0.45$ . This suggests that orogenic wedges seem to be in a critical  
 809 state when  $E_F \approx 0.45$ . Thus the evolution of an orogenic system should be non-linear.  
 810

#### 811 5.4 The mechanism of the formation of the eastern Himalayan syntaxis

812 All the three classical models explaining the formation of syntaxis have undergone extensive  
 813 testing through abundant field observations and numerical modeling studies (Bendick & Ehlers,  
 814 2014; Burg et al., 1998; Burg & Podladchikov, 1999; Burg & Schmalholz, 2008; Ding et al.,  
 815 2001; Koons et al., 2002; Koptev et al., 2019; Nettesheim et al., 2018; Yang et al., 2023; Zeitler,  
 816 Koons, et al., 2001; Zeitler et al., 2014; Zhang et al., 2004). Our modelling results indicate that  
 817 the processes involved in the formation of syntaxis are more closely associated with those

818 described by the tectonic aneurysm model (Figure 8 and 9), and we propose that the initiation of  
 819 these processes requires the cooperation of tectonic forces, climatic forces and geothermal field  
 820 (Figure 15).  
 821



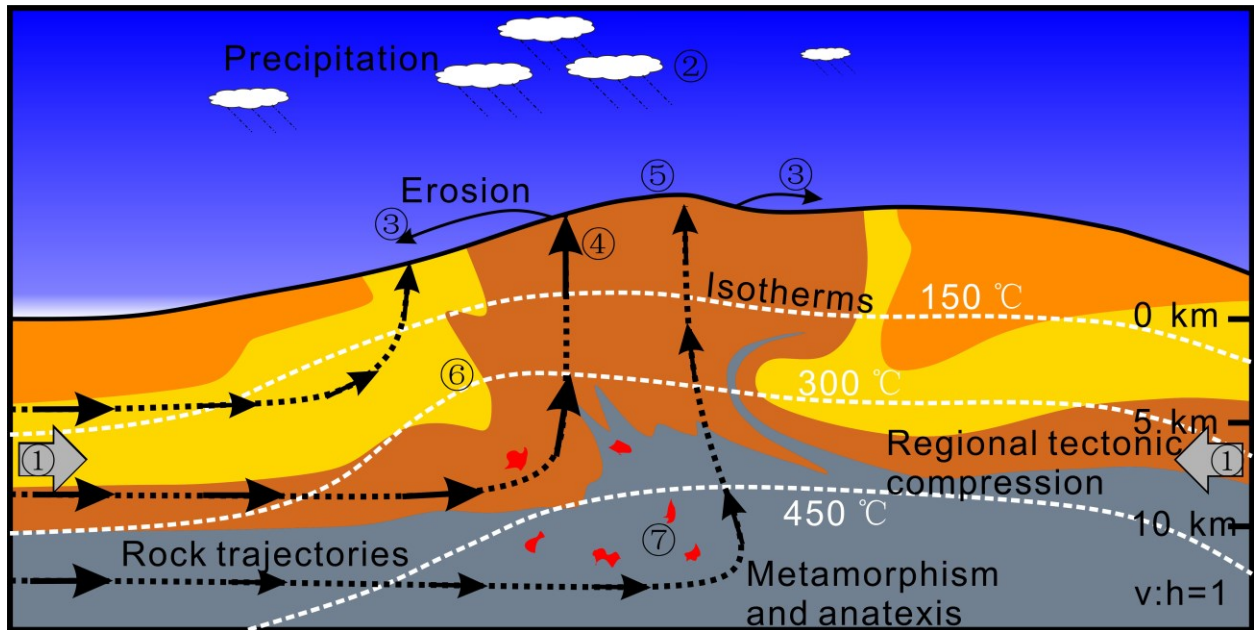
822  
 823 **Figure 15.** The proposed mechanism of the formation of the eastern Himalayan syntaxis. The  
 824 elements outside the red dashed circle are the conditions for the formation of a syntaxis, while  
 825 the elements inside the red dashed circle show the process of its formation. The formation of a  
 826 syntaxis requires the combination of tectonic forces, climatic forces and crustal thermal structure.  
 827 Once the convergence rate and the average precipitation fall within the Type D zone  
 828 determined by the thermal structure of shallow crust, a sustained, stationary, localized and relatively rapid  
 829 erosion process will be established on the windward flank of the orogenic wedge. This will  
 830 further induce sustained and rapid uplift of rocks, exhumation and deformation, ultimately  
 831 forming a syntaxis.  
 832

833 For a given crust, it may have a Type D zone, which is determined by its thermal structure  
 834 (Figure 7). In addition, a certain degree of regional tectonic compression (or crustal shortening)  
 835 and precipitation, including the resultant erosion, are also necessary. During the orogenesis,

836 regional tectonic compression sets the initial conditions by raising Earth's surface. If moisture is  
837 transported into the region by the prevailing winds, it will lead to longitudinal (perpendicular to  
838 the strike of the mountain range) localization of precipitation (Anders et al., 2006; Berger &  
839 Spotila, 2008; Burbank et al., 2003; Reiners et al., 2003; Roe, 2005; Roe et al., 2002; Wratt et al.,  
840 2000) (Figure 15 path A, Figure 10a). At the same time, precipitation is also influenced by other  
841 factors such as latitude, continentality, and topographic features (Barry, 2008), which can lead to  
842 spatial heterogeneity of precipitation in the direction parallel to the strike of the mountain range,  
843 namely lateral localization of precipitation (Anders et al., 2006; Bookhagen & Burbank, 2006)  
844 (Figure 15 path B). The superposition of these two effects will lead to point-like precipitation  
845 enhancement within mountain belts. If the average precipitation and convergence rate fall within  
846 the Type D zone, a sustained, stationary, localized and relatively rapid erosion process will be  
847 established on the windward flank (Figure 9). This will further induce sustained and rapid uplift  
848 of rocks, exhumation and deformation (Figure 9, Figure 11, Figure 15 path C), ultimately leading  
849 to the formation of a large-scale antiform. At the core area of the antiform, extreme relief, deep  
850 exhumation, intense deformation and steepening of the near-surface thermal gradient overlap  
851 spatially. Additionally, the crustal material may experience low-P-high-T metamorphism and  
852 decompression melting during rapid uplifting and exhumation (Booth et al., 2009; Booth et al.,  
853 2004; Koons et al., 2002; Koons et al., 2013; Zeitler, Meltzer, et al., 2001) (Figure 17). Here,  
854 "sustained" means that the formation of a mature syntaxis needs a certain amount of time.  
855 According to our modelling, this process takes several million years. During this period, the  
856 average precipitation and convergence rate need to remain relatively stable (not falling outside  
857 the Type D zone). "Stationary" and "localized" mean that the position of the intense erosion zone  
858 on the windward flank do not undergo significant changes (Figure 9, Figure 11). "Relatively  
859 rapid" means that the erosional efficiency cannot be too fast (which would rapidly flatten the  
860 topography) nor too slow (which would cause continuous of deformation towards the foreland  
861 basin and lead to the displacement of the position of the intense erosion zone). Instead, it should  
862 be moderate to allow the majority of the material entering the orogenic wedge "flows out"  
863 through the narrow erosional window (Figure 11, Figure 16), so that this state can be maintained  
864 relatively stable over the long term (several million years).

865 In this context, the process of rock uplift triggered by erosion is governed by the universal  
866 principle that natural systems have the tendency towards dynamic equilibrium (Hack, 1975). The  
867 dynamic equilibrium of an orogen can be expressed as relatively stable states of material flux,  
868 topography, geotherm and exhumation (Willett & Brandon, 2002). In essence, it's about the  
869 equilibrium of temperature and pressure within the orogenic system. Rapid erosion can cause  
870 perturbations in the orogenic system, resulting in imbalances in temperature and pressure. To  
871 achieve a new state of equilibrium, the orogen will respond to the perturbations by undergoing  
872 rapid uplift, exhumation, deformation and steepening of geothermal gradients. Satellite rainfall  
873 estimates indicate that heaviest rainfall amounts within Himalayas occur closer to the major  
874 moisture source, the two ends of the Himalayan arc (Anders et al., 2006; Bookhagen & Burbank,  
875 2006). Such precipitation localization effect might have resulted in the average precipitation and  
876 convergence rates at two ends of the Himalayan arc falling within their Type D zones, thereby  
877 promoting the development of syntaxes. The east-west rainfall gradient in the Himalayas is  
878 mainly influenced by the shape of Indian subcontinent, which has contributed to its stability  
879 since the onset of the Indian and east Asian monsoons (8-9 Ma) (Zhisheng et al., 2001).  
880 Meanwhile, the shortening rate of the Himalayas has remained relatively stable since 40 Ma

881 (Guillot et al., 2003), providing relatively stable tectonic and climatic conditions for the  
 882 development of a mature syntaxis.  
 883



884  
 885 **Figure 16.** Geologic manifestation of a mature syntaxis. Once the convergence rate(①) and the  
 886 average precipitation(②) fall within the Type D zone determined by the thermal structure of  
 887 shallow crust, the formation process of a syntaxis will be initiated. Subsequently, a sustained,  
 888 stationary, localized and relatively rapid erosion process(③) will be established on the windward  
 889 flank of the orogenic wedge. This erosion process further induces sustained and rapid uplift of  
 890 rocks, deep exhumation and intense deformation(④) within the intense erosion zone, forming  
 891 large-scale antiform. Within the core of the antiform, extreme relief(⑤), deep exhumation,  
 892 intense deformation and steepening of the near-surface thermal gradient(⑥) overlap spatially.  
 893 During rapid uplifting and exhumation, crustal material may experience low-P-high-T  
 894 metamorphism and decompression melting(⑦).

895  
 896 In model S034 and other type D models, there are no obvious low-viscosity channels  
 897 observed near the intense erosion zone on the windward flank of the orogenic wedge (Figure 11).  
 898 Therefore, we suspect that the positive feedback among erosion, heat advection, rock strength  
 899 and deformation may not be necessary during the development of syntaxis. However, strain  
 900 concentration and steepening of geothermal gradients will inevitably reduce rock viscosity in  
 901 some degree (Ranalli, 1995; Turcotte & Schubert, 2014) so that the positive feedback is  
 902 theoretically possible (Koons et al., 2002; Yang et al., 2023). In our models, the positive  
 903 feedback was not observed possibly due to our model simplifications.

904 The complex interplay among climate, tectonics and surface processes in the orogen  
 905 implies that orogen is best viewed as complex open system controlled by multiple factors (Pinter  
 906 & Brandon, 1997). The system always evolves towards dynamic equilibrium and responds to  
 907 changes in controlling factors in order to achieve a new state of equilibrium (Molnar, 2009). The  
 908 response of the orogenic system to a specific factor also depends on the other controlling factors.  
 909 Therefore, the evolution of an orogen is determined by a series of controlling factors (system

910 inputs), none of which can be considered as the sole cause of the system's outcome. In mountain  
911 belts, once the convergence rate and the average precipitation fall within the Type D zone  
912 determined by the crustal thermal structure, syntaxis becomes the inevitable system's outcome  
913 under various physical laws, including conservation of mass, momentum and energy, rheology,  
914 orographic precipitation, surface processes, etc.

## 915 **5 Conclusions**

916 We presented results from numerical experiments that explore the interactions between  
917 climate, tectonics and surface processes, as well as the formation conditions and mechanisms of  
918 the eastern Himalayan syntaxis. In this study, we have tested three crucial controlling  
919 parameters: the convergence rate, average precipitation and initial geothermal gradient.  
920 Combined with field observations, we draw the following conclusions:

- 921 1. For a specific orogenic wedge, its tectonic and topographic evolution primarily relies on the  
922 relative strength of tectonic and climatic forces, rather than their respective magnitudes. When  
923 the tectonic forces are relatively stronger, the orogenic wedge tends to broaden, increase in  
924 elevation, and develop thrust faults. Conversely, when the tectonic forces are relatively weaker,  
925 the orogenic wedge tends to narrow, decrease in elevation, and develop folds.
- 926 2. For a specific orogenic wedge, there may exist a Type D zone in the in the  $P_0 - v_c$  parameter  
927 space. This Type D zone is determined by the thermal structure of the crust, and its presence is  
928 the necessary condition for the development of a syntaxis.
- 929 3. Orogens are best viewed as complex open systems controlled by multiple factors. A syntaxis  
930 is the result of the combined effects of tectonic forces, climatic forces and geothermal field. In  
931 mountain belts, once the convergence rate and the average precipitation fall within the Type D  
932 zone, syntaxis becomes the inevitable system's outcome under various physical laws, including  
933 conservation of mass, momentum and energy, rheology, orographic precipitation, surface  
934 processes, etc.

## 935 **Acknowledgments**

936 This research has been funded by the National Natural Science Foundation of China (Grants  
937 Nos. 40472100, and 41472175). We are indebted to Prof. Taras Gerya for generously sharing the  
938 finite difference code used for thermo-mechanical calculations. We also express our gratitude to  
939 Daniel E. J. Hobley, Katherine R. Barnhart and their team for granting us access to landlab  
940 software for landscape evolution modelling.

941

## 942 **Data Availability Statement**

943 The finite difference code used for thermo-mechanical calculations can be found at  
944 [www.cambridge.org/gerya2e](http://www.cambridge.org/gerya2e). The landlab source code is found at  
945 <https://github.com/landlab/landlab>. Figures are plotted by MATLAB and Python.

946

## 947 **References**

948 Anders, A. M., Roe, G. H., Hallet, B., Montgomery, D. R., Finnegan, N. J., & Putkonen, J. (2006). Spatial patterns  
949 of precipitation and topography in the Himalaya. *Special Papers-Geological Society of America*, 398, 39.

- 950 Avouac, J.-P., & Burov, E. (1996). Erosion as a driving mechanism of intracontinental mountain growth. *Journal of*  
951 *Geophysical Research: Solid Earth*, *101*(B8), 17747-17769.
- 952 Bahadori, A., Holt, W. E., Feng, R., Austermann, J., Loughney, K. M., Salles, T., . . . Flesch, L. M. (2022). Coupled  
953 influence of tectonics, climate, and surface processes on landscape evolution in southwestern North  
954 America. *Nature communications*, *13*(1), 4437.
- 955 Barnhart, K. R., Glade, R. C., Shobe, C. M., & Tucker, G. E. (2019). Terrainbento 1.0: a Python package for multi-  
956 model analysis in long-term drainage basin evolution. *Geoscientific Model Development*, *12*(4), 1267-1297.
- 957 Barnhart, K. R., Hutton, E. W., Tucker, G. E., Gasparini, N. M., Istanbuluoglu, E., Hobley, D. E., . . . Adams, J. M.  
958 (2020). Landlab v2. 0: A software package for Earth surface dynamics. *Earth Surface Dynamics*, *8*(2), 379-  
959 397.
- 960 Barros, A. P., & Lettenmaier, D. P. (1994). Dynamic modeling of orographically induced precipitation. *Reviews of*  
961 *geophysics*, *32*(3), 265-284.
- 962 Barry, R. (2008). Mountain weather and climate. Cambridge University Press. *New York*.
- 963 Beaumont, C., Jamieson, R. A., Nguyen, M., & Lee, B. (2001). Himalayan tectonics explained by extrusion of a  
964 low-viscosity crustal channel coupled to focused surface denudation. *Nature*, *414*(6865), 738-742.
- 965 Beaumont, C., Jamieson, R. A., Nguyen, M. H., & Medvedev, S. (2004). Crustal channel flows: 1. Numerical  
966 models with applications to the tectonics of the Himalayan - Tibetan orogen. *Journal of Geophysical*  
967 *Research: Solid Earth*, *109*(B6).
- 968 Bendick, R., & Ehlers, T. A. (2014). Extreme localized exhumation at syntaxes initiated by subduction geometry.  
969 *Geophysical Research Letters*, *41*(16), 5861-5867.
- 970 Berger, A. L., Gulick, S. P., Spotila, J. A., Upton, P., Jaeger, J. M., Chapman, J. B., . . . Willems, B. A. (2008).  
971 Quaternary tectonic response to intensified glacial erosion in an orogenic wedge. *Nature geoscience*, *1*(11),  
972 793-799.
- 973 Berger, A. L., & Spotila, J. A. (2008). Denudation and deformation in a glaciated orogenic wedge: The St. Elias  
974 orogen, Alaska. *Geology*, *36*(7), 523-526.
- 975 Bookhagen, B., & Burbank, D. W. (2006). Topography, relief, and TRMM - derived rainfall variations along the  
976 Himalaya. *Geophysical Research Letters*, *33*(8).
- 977 Booth, A. L., Chamberlain, C. P., Kidd, W. S., & Zeitler, P. K. (2009). Constraints on the metamorphic evolution of  
978 the eastern Himalayan syntaxis from geochronologic and petrologic studies of Namche Barwa. *Geological*  
979 *Society of America Bulletin*, *121*(3-4), 385-407.
- 980 Booth, A. L., Zeitler, P. K., Kidd, W. S., Wooden, J., Liu, Y., Idleman, B., . . . Chamberlain, C. P. (2004). U-Pb  
981 zircon constraints on the tectonic evolution of southeastern Tibet, Namche Barwa area. *American journal of*  
982 *Science*, *304*(10), 889-929.
- 983 Bracciali, L., Parrish, R. R., Najman, Y., Smye, A., Carter, A., & Wijbrans, J. R. (2016). Plio-Pleistocene  
984 exhumation of the eastern Himalayan syntaxis and its domal 'pop-up'. *Earth-Science Reviews*, *160*, 350-  
985 385.
- 986 Buitter, S. J. (2012). A review of brittle compressional wedge models. *Tectonophysics*, *530*, 1-17.
- 987 Burbank, D., Blythe, A., Putkonen, J., Pratt-Sitaula, B., Gabet, E., Oskin, M., . . . Ojha, T. (2003). Decoupling of  
988 erosion and precipitation in the Himalayas. *Nature*, *426*(6967), 652-655.
- 989 Burg, J.-P., Nievergelt, P., Oberli, F., Seward, D., Davy, P., Maurin, J.-C., . . . Meier, M. (1998). The Namche  
990 Barwa syntaxis: evidence for exhumation related to compressional crustal folding. *Journal of Asian Earth*  
991 *Sciences*, *16*(2-3), 239-252.
- 992 Burg, J.-P., & Podladchikov, Y. (1999). Lithospheric scale folding: numerical modelling and application to the  
993 Himalayan syntaxes. *International Journal of Earth Sciences*, *88*(2), 190-200.
- 994 Burg, J.-P., & Schmalholz, S. (2008). Viscous heating allows thrusting to overcome crustal-scale buckling:  
995 Numerical investigation with application to the Himalayan syntaxes. *Earth and Planetary Science Letters*,  
996 *274*(1-2), 189-203.
- 997 Burg, J. P., Davy, P., Nievergelt, P., Oberli, F., Seward, D., Diao, Z., & Meier, M. (1997). Exhumation during  
998 crustal folding in the Namche - Barwa syntaxis. *Terra Nova*, *9*(2), 53-56.
- 999 Butler, R. W. (2019). Tectonic evolution of the Himalayan syntaxes: the view from Nanga Parbat. *Geological*  
1000 *Society, London, Special Publications*, *483*(1), 215-254.
- 1001 Butler, R. W. H., Casey, M., Lloyd, G. E., Bond, C. E., McDade, P., Shipton, Z., & Jones, R. (2002). Vertical  
1002 stretching and crustal thickening at Nanga Parbat, Pakistan Himalaya: a model for distributed continental  
1003 deformation during mountain building. *Tectonics*, *21*(4), 9-1-9-17.

- 1004 Champagnac, J. D., Molnar, P., Sue, C., & Herman, F. (2012). Tectonics, climate, and mountain topography.  
1005 *Journal of Geophysical Research: Solid Earth*, 117(B2).
- 1006 Champagnac, J. D., Valla, P. G., & Herman, F. (2014). Late-Cenozoic relief evolution under evolving climate: A  
1007 review. *Tectonophysics*, 614(1), 44-65.
- 1008 Clift, P. D., Pandey, D. K., & Kulhanek, D. K. (2020). Climate–tectonic interactions in the eastern Arabian Sea.  
1009 *Geological Magazine*, 157(6), 829-833.
- 1010 Cramer, F., Schmeling, H., Golabek, G., Duretz, T., Orendt, R., Buitter, S., . . . Tackley, P. (2012). A comparison of  
1011 numerical surface topography calculations in geodynamic modelling: an evaluation of the ‘sticky  
1012 air’ method. *Geophysical Journal International*, 189(1), 38-54.
- 1013 Craw, D., Koons, P., Zeitler, P., & Kidd, W. (2005). Fluid evolution and thermal structure in the rapidly exhuming  
1014 gneiss complex of Namche Barwa–Gyala Peri, eastern Himalayan syntaxis. *Journal of Metamorphic  
1015 Geology*, 23(9), 829-845.
- 1016 Cruz, L., Malinski, J., Wilson, A., Take, W., & Hilley, G. (2010). Erosional control of the kinematics and geometry  
1017 of fold - and - thrust belts imaged in a physical and numerical sandbox. *Journal of Geophysical Research:  
1018 Solid Earth*, 115(B9).
- 1019 Culling, W. (1963). Soil creep and the development of hillside slopes. *The Journal of Geology*, 71(2), 127-161.
- 1020 Dadson, S. J., Hovius, N., Chen, H., Dade, W. B., Hsieh, M.-L., Willett, S. D., . . . Stark, C. P. (2003). Links  
1021 between erosion, runoff variability and seismicity in the Taiwan orogen. *Nature*, 426(6967), 648-651.
- 1022 Dahlen, F. (1990). Critical taper model of fold-and-thrust belts and accretionary wedges. *Annual Review of Earth  
1023 and Planetary Sciences*, 18(1), 55-99.
- 1024 Dahlen, F., Suppe, J., & Clark, S. (1988). Mechanics, growth, and erosion of mountain belts. *Processes in  
1025 continental lithospheric deformation*, 218, 161-178.
- 1026 Davy, P., & Lague, D. (2009). Fluvial erosion/transport equation of landscape evolution models revisited. *Journal of  
1027 Geophysical Research: Earth Surface*, 114(F3).
- 1028 Ding, L., Zhong, D., Yin, A., Kapp, P., & Harrison, T. M. (2001). Cenozoic structural and metamorphic evolution of  
1029 the eastern Himalayan syntaxis (Namche Barwa). *Earth and Planetary Science Letters*, 192(3), 423-438.
- 1030 Egholm, D., Nielsen, S., Pedersen, V., & Lesemann, J.-E. (2009). Glacial effects limiting mountain height. *Nature*,  
1031 460(7257), 884-887.
- 1032 Emanuel, K. A. (1994). *Atmospheric convection*. Oxford University Press on Demand.
- 1033 Enkelmann, E., Ehlers, T., Zeitler, P., & Hallet, B. (2011). Denudation of the Namche Barwa antiform, eastern  
1034 Himalaya. *Earth and Planetary Science Letters*, 307(3-4), 323-333.
- 1035 Fernandes, N. F., & Dietrich, W. E. (1997). Hillslope evolution by diffusive processes: The timescale for  
1036 equilibrium adjustments. *Water Resources Research*, 33(6), 1307-1318.
- 1037 Finnegan, N. J., Hallet, B., Montgomery, D. R., Zeitler, P. K., Stone, J. O., Anders, A. M., & Yuping, L. (2008).  
1038 Coupling of rock uplift and river incision in the Namche Barwa–Gyala Peri massif, Tibet. *Geological  
1039 Society of America Bulletin*, 120(1-2), 142-155.
- 1040 Gerya, T. (2019). *Introduction to numerical geodynamic modelling*. Cambridge University Press.
- 1041 Gong, J., Ji, J., Zhou, J., Tu, J., Sun, D., Zhong, D., & Han, B. (2015). Late Miocene thermal evolution of the eastern  
1042 Himalayan syntaxis as constrained by biotite 40Ar/39Ar thermochronology. *The Journal of Geology*,  
1043 123(4), 369-384.
- 1044 Grujic, D., Coutand, I., Bookhagen, B., Bonnet, S., Blythe, A., & Duncan, C. (2006). Climatic forcing of erosion,  
1045 landscape, and tectonics in the Bhutan Himalayas. *Geology*, 34(10), 801-804.
- 1046 Guillot, S., Garzanti, E., Baratoux, D., Marquer, D., Mahéo, G., & de Sigoyer, J. (2003). Reconstructing the total  
1047 shortening history of the NW Himalaya. *Geochemistry, Geophysics, Geosystems*, 4(7).
- 1048 Hack, J. T. (1957). *Studies of longitudinal stream profiles in Virginia and Maryland* (Vol. 294). US Government  
1049 Printing Office.
- 1050 Hack, J. T. (1975). Dynamic equilibrium and landscape evolution. *Theories of landform development*, 1, 87-102.
- 1051 Herman, F., Seward, D., Valla, P. G., Carter, A., Kohn, B., Willett, S. D., & Ehlers, T. A. (2013). Worldwide  
1052 acceleration of mountain erosion under a cooling climate. *Nature*, 504(7480), 423-426.
- 1053 Hilley, G., Strecker, M., & Ramos, V. (2004). Growth and erosion of fold - and - thrust belts with an application to  
1054 the Aconcagua fold - and - thrust belt, Argentina. *Journal of Geophysical Research: Solid Earth*, 109(B1).
- 1055 Hogley, D. E., Adams, J. M., Nudurupati, S. S., Hutton, E. W., Gasparini, N. M., Istanbuloglu, E., & Tucker, G. E.  
1056 (2017). Creative computing with Landlab: an open-source toolkit for building, coupling, and exploring  
1057 two-dimensional numerical models of Earth-surface dynamics. *Earth Surface Dynamics*, 5(1), 21-46.

- 1058 King, G. E., Herman, F., & Guralnik, B. (2016). Northward migration of the eastern Himalayan syntaxis revealed by  
1059 OSL thermochronometry. *Science*, 353(6301), 800-804.
- 1060 Koons, P. (1995). Modeling the topographic evolution of collisional belts. *Annual Review of Earth and Planetary  
1061 Sciences*, 23(1), 375-408.
- 1062 Koons, P., Zeitler, P., Chamberlain, C., Craw, D., & Meltzer, A. (2002). Mechanical links between erosion and  
1063 metamorphism in Nanga Parbat, Pakistan Himalaya. *American journal of Science*, 302(9), 749-773.
- 1064 Koons, P. O., Zeitler, P. K., & Hallet, B. (2013). Tectonic Aneurysms and Mountain Building. In J. F. Shroder (Ed.),  
1065 *Treatise on geomorphology* (pp. 318-349). Academic Press. [https://doi.org/https://doi.org/10.1016/B978-0-  
1066 12-374739-6.00094-4](https://doi.org/10.1016/B978-0-12-374739-6.00094-4)
- 1067 Koptev, A., Ehlers, T. A., Nettesheim, M., & Whipp, D. M. (2019). Response of a rheologically stratified  
1068 lithosphere to subduction of an indenter - shaped plate: Insights into localized exhumation at orogen  
1069 syntaxes. *Tectonics*, 38(6), 1908-1930.
- 1070 Lin, T.-H., Lo, C.-H., Chung, S.-L., Hsu, F.-J., Yeh, M.-W., Lee, T.-Y., . . . Liu, D. (2009). 40Ar/39Ar dating of the  
1071 Jiali and Gaoligong shear zones: Implications for crustal deformation around the Eastern Himalayan  
1072 Syntaxis. *Journal of Asian Earth Sciences*, 34(5), 674-685.
- 1073 Liu, Y., & Zhong, D. (1997). Petrology of high - pressure granulites from the eastern Himalayan syntaxis. *Journal  
1074 of Metamorphic Geology*, 15(4), 451-466.
- 1075 Molnar, P. (2003). Nature, nurture and landscape. *Nature*, 426(6967), 612-613.
- 1076 Molnar, P. (2009). The state of interactions among tectonics, erosion, and climate: A polemic. *GSA Today*, 19(7),  
1077 44-45.
- 1078 Molnar, P., & England, P. (1990). Late Cenozoic uplift of mountain ranges and global climate change: chicken or  
1079 egg? *Nature*, 346(6279), 29-34.
- 1080 Montgomery, D. R., & Dietrich, W. E. (1992). Channel initiation and the problem of landscape scale. *Science*,  
1081 255(5046), 826-830.
- 1082 Mukhopadhyay, B., Acharyya, A., Bhattacharyya, D., Dasgupta, S., & Pande, P. (2011). Seismotectonics at the  
1083 terminal ends of the Himalayan arc. *Geomatics, Natural Hazards and Risk*, 2(2), 159-181.
- 1084 NASEM. (2020). *A vision for NSF Earth sciences 2020-2030: Earth in time*. National Academies Press.
- 1085 Nettesheim, M., Ehlers, T. A., Whipp, D. M., & Koptev, A. (2018). The influence of upper-plate advance and  
1086 erosion on overriding plate deformation in orogen syntaxes. *Solid Earth*, 9(6), 1207-1224.
- 1087 Norton, K., & Schlunegger, F. (2011). Migrating deformation in the Central Andes from enhanced orographic  
1088 rainfall. *Nature communications*, 2(1), 1-7.
- 1089 Peizhen, Z., Molnar, P., & Downs, W. R. (2001). Increased sedimentation rates and grain sizes 2–4 Myr ago due to  
1090 the influence of climate change on erosion rates. *Nature*, 410(6831), 891-897.
- 1091 Phillips, C. L., Parr, J. M., Riskin, E. A., & Prabhakar, T. (2003). *Signals, systems, and transforms*. Prentice Hall  
1092 Upper Saddle River.
- 1093 Pinter, N., & Brandon, M. T. (1997). How erosion builds mountains. *Scientific American*, 276(4), 74-79.
- 1094 Ranalli, G. (1995). *Rheology of the Earth*. Springer Science & Business Media.
- 1095 Raymo, M. E., & Ruddiman, W. F. (1992). Tectonic forcing of late Cenozoic climate. *Nature*, 359(6391), 117-122.
- 1096 Reiners, P. W., Ehlers, T. A., Mitchell, S. G., & Montgomery, D. R. (2003). Coupled spatial variations in  
1097 precipitation and long-term erosion rates across the Washington Cascades. *Nature*, 426(6967), 645-647.
- 1098 Roe, G. H. (2005). Orographic precipitation. *Annu. Rev. Earth Planet. Sci.*, 33, 645-671.
- 1099 Roe, G. H., Montgomery, D. R., & Hallet, B. (2002). Effects of orographic precipitation variations on the concavity  
1100 of steady-state river profiles. *Geology*, 30(2), 143-146.
- 1101 Roe, G. H., Stolar, D. B., & Willett, S. D. (2006). Response of a steady-state critical wedge orogen to changes in  
1102 climate and tectonic forcing. *Special Papers-Geological Society of America*, 398, 227.
- 1103 Roe, G. H., Whipple, K. X., & Fletcher, J. K. (2008). Feedbacks among climate, erosion, and tectonics in a critical  
1104 wedge orogen. *American journal of Science*, 308(7), 815-842.
- 1105 Royden, L. H., Burchfiel, B. C., & van der Hilst, R. D. (2008). The geological evolution of the Tibetan Plateau.  
1106 *Science*, 321(5892), 1054-1058.
- 1107 Ruh, J. B., Kaus, B. J., & Burg, J. P. (2012). Numerical investigation of deformation mechanics in fold - and -  
1108 thrust belts: Influence of rheology of single and multiple décollements. *Tectonics*, 31(3).
- 1109 Schmeling, H., Babeyko, A., Enns, A., Faccenna, C., Funicello, F., Gerya, T., . . . Morra, G. (2008). A benchmark  
1110 comparison of spontaneous subduction models—Towards a free surface. *Physics of the Earth and  
1111 Planetary Interiors*, 171(1-4), 198-223.

- 1112 Schulte-Pelkum, V., Monsalve, G., Sheehan, A., Pandey, M., Sapkota, S., Bilham, R., & Wu, F. (2005). Imaging the  
1113 Indian subcontinent beneath the Himalaya. *Nature*, *435*(7046), 1222-1225.
- 1114 Seward, D., & Burg, J.-P. (2008). Growth of the Namche Barwa Syntaxis and associated evolution of the Tsangpo  
1115 Gorge: Constraints from structural and thermochronological data. *Tectonophysics*, *451*(1-4), 282-289.
- 1116 Simpson, G. (2004). Role of river incision in enhancing deformation. *Geology*, *32*(4), 341-344.
- 1117 Smith, R., & Barstad, I. (2004). A Linear Theory of Orographic Precipitation. *Journal of The Atmospheric Sciences*  
1118 - *JATMOS SCI*, *61*, 1377-1391. [https://doi.org/10.1175/1520-0469\(2004\)061<1377:ALTOOP>2.0.CO;2](https://doi.org/10.1175/1520-0469(2004)061<1377:ALTOOP>2.0.CO;2)
- 1119 Song, Z., Zhenhan, W., Xitao, Z., Jianping, L., & Hua, W. (2012). Middle-Late Pleistocene Glacial Lakes in the  
1120 Grand Canyon of the Tsangpo River, Tibet. *Acta Geologica Sinica - English Edition*, *86*(1), 266-283.  
1121 <https://doi.org/https://doi.org/10.1111/j.1755-6724.2012.00627.x>
- 1122 Steer, P., Simoes, M., Cattin, R., & Shyu, J. B. H. (2014). Erosion influences the seismicity of active thrust faults.  
1123 *Nature communications*, *5*(1), 1-7.
- 1124 Stewart, R., Hallet, B., Zeitler, P., Malloy, M., Allen, C. M., & Trippett, D. (2008). Brahmaputra sediment flux  
1125 dominated by highly localized rapid erosion from the easternmost Himalaya. *Geology*, *36*(9), 711-714.
- 1126 Stolar, D. B., Willett, S. D., & Roe, G. H. (2006). Climatic and tectonic forcing of a critical orogen. *Special Papers-*  
1127 *Geological Society of America*, *398*, 241.
- 1128 Tapponnier, P., Zhiqin, X., Roger, F., Meyer, B., Arnaud, N., Wittlinger, G., & Jingsui, Y. (2001). Oblique stepwise  
1129 rise and growth of the Tibet Plateau. *Science*, *294*(5547), 1671-1677.
- 1130 Tomkin, J. H., & Roe, G. H. (2007). Climate and tectonic controls on glaciated critical-taper orogens. *Earth and*  
1131 *Planetary Science Letters*, *262*(3-4), 385-397.
- 1132 Tu, J.-Y., Ji, J.-Q., Sun, D.-X., Gong, J.-F., Zhong, D.-L., & Han, B.-F. (2015). Thermal structure, rock exhumation,  
1133 and glacial erosion of the Namche Barwa Peak, constraints from thermochronological data. *Journal of*  
1134 *Asian Earth Sciences*, *105*, 223-233.
- 1135 Turcotte, D., & Schubert, G. (2014). Geodynamics.
- 1136 Valla, P. G., Sternai, P., & Fox, M. (2021). How climate, uplift and erosion shaped the Alpine topography.  
1137 *Elements: An International Magazine of Mineralogy, Geochemistry, and Petrology*, *17*(1), 41-46.
- 1138 Vogt, K., Matenco, L., & Cloetingh, S. (2017). Crustal mechanics control the geometry of mountain belts. Insights  
1139 from numerical modelling. *Earth and Planetary Science Letters*, *460*, 12-21.  
1140 <https://doi.org/https://doi.org/10.1016/j.epsl.2016.11.016>
- 1141 Vogt, K., Willingshofer, E., Matenco, L., Sokoutis, D., Gerya, T., & Cloetingh, S. (2018). The role of lateral  
1142 strength contrasts in orogenesis: A 2D numerical study. *Tectonophysics*, *746*, 549-561.
- 1143 Wang, P., Scherler, D., Liu-Zeng, J., Mey, J., Avouac, J.-P., Zhang, Y., & Shi, D. (2014). Tectonic control of  
1144 Yarlung Tsangpo Gorge revealed by a buried canyon in Southern Tibet. *Science*, *346*(6212), 978-981.
- 1145 Whipp Jr, D. M., Beaumont, C., & Braun, J. (2014). Feeding the “aneurysm”: Orogen - parallel mass transport into  
1146 Nanga Parbat and the western Himalayan syntaxis. *Journal of Geophysical Research: Solid Earth*, *119*(6),  
1147 5077-5096.
- 1148 Whipple, K. X. (2009). The influence of climate on the tectonic evolution of mountain belts. *Nature geoscience*,  
1149 *2*(2), 97-104.
- 1150 Whipple, K. X. (2014). Can erosion drive tectonics? *Science*, *346*(6212), 918-919.
- 1151 Whipple, K. X., & Meade, B. J. (2004). Controls on the strength of coupling among climate, erosion, and  
1152 deformation in two - sided, frictional orogenic wedges at steady state. *Journal of Geophysical Research:*  
1153 *Earth Surface*, *109*(F1).
- 1154 Whipple, K. X., & Meade, B. J. (2006). Orogen response to changes in climatic and tectonic forcing. *Earth and*  
1155 *Planetary Science Letters*, *243*(1-2), 218-228.
- 1156 Whipple, K. X., & Tucker, G. E. (1999). Dynamics of the stream - power river incision model: Implications for  
1157 height limits of mountain ranges, landscape response timescales, and research needs. *Journal of*  
1158 *Geophysical Research: Solid Earth*, *104*(B8), 17661-17674.
- 1159 Willett, S. D. (1999). Orogeny and orography: The effects of erosion on the structure of mountain belts. *Journal of*  
1160 *Geophysical Research: Solid Earth*, *104*(B12), 28957-28981.
- 1161 Willett, S. D. (2006). *Tectonics, climate, and landscape evolution* (Vol. 398). Geological Society of America.
- 1162 Willett, S. D., & Brandon, M. T. (2002). On steady states in mountain belts. *Geology*, *30*(2), 175-178.
- 1163 Willett, S. D., Schlunegger, F., & Picotti, V. (2006). Messinian climate change and erosional destruction of the  
1164 central European Alps. *Geology*, *34*(8), 613-616.
- 1165 Wolf, S. G., Huismans, R. S., Braun, J., & Yuan, X. (2022). Topography of mountain belts controlled by rheology  
1166 and surface processes. *Nature*, 1-6.

- 1167 Wratt, D., Revell, M., Sinclair, M., Gray, W., Henderson, R., & Chater, A. (2000). Relationships between air mass  
1168 properties and mesoscale rainfall in New Zealand's Southern Alps. *Atmospheric Research*, 52(4), 261-282.
- 1169 Xiangjiang, W. F. J. J. Y., & Dalai, T. J. Z. (2017). Quantitative research on temporal and spatial coupling of  
1170 precipitation potential energy and erosion intensity in Himalayas. *Chinese Journal of Geology*, 52(1), 1-14.
- 1171 Yang, J., Cao, W., Yuan, X., & Yang, J. (2023). Erosion-Driven Isostatic Flow and Crustal Diapirism: Analytical  
1172 and Numerical Models With Implications for the Evolution of the Eastern Himalayan Syntaxis, Southern  
1173 Tibet. *Tectonics*, 42(8), e2022TC007717. <https://doi.org/https://doi.org/10.1029/2022TC007717>
- 1174 Yang, R., Herman, F., Fellin, M. G., & Maden, C. (2018). Exhumation and topographic evolution of the Namche  
1175 Barwa Syntaxis, eastern Himalaya. *Tectonophysics*, 722, 43-52.
- 1176 Yao, T., Li, Z., Yang, W., Guo, X., Zhu, L., Kang, S., . . . Yu, W. (2010). Glacial distribution and mass balance in  
1177 the Yarlung Zangbo River and its influence on lakes. *Chinese Science Bulletin*, 55(20), 2072-2078.
- 1178 Ye, Y., Wu, L., Cowgill, E., Tian, Y., Lin, X., Xiao, A., & Chen, H. (2022). Long-lagged (~ 19 Myr) response of  
1179 accelerated river incision to rock uplift on the northern margin of the Tibetan Plateau. *Earth and Planetary  
1180 Science Letters*, 591, 117608.
- 1181 Yin, A. (2006). Cenozoic tectonic evolution of the Himalayan orogen as constrained by along-strike variation of  
1182 structural geometry, exhumation history, and foreland sedimentation. *Earth-Science Reviews*, 76(1-2), 1-  
1183 131.
- 1184 Yu, X., Ji, J., Gong, J., Sun, D., Qing, J., Wang, L., . . . Zhang, Z. (2011). Evidences of rapid erosion driven by  
1185 climate in the Yarlung Zangbo (Tsangpo) Great Canyon, the eastern Himalayan syntaxis. *Chinese Science  
1186 Bulletin*, 56(11), 1123-1130. <https://doi.org/10.1007/s11434-011-4419-x>
- 1187 Yu, X., Ji, J., Wang, F., & Zhong, D. (2017). Intensified climate-driven exhumation along the South Himalayan  
1188 Front since one million years ago. *Journal of Asian Earth Sciences*, 136, 50-57.
- 1189 Yuan, X. P., Braun, J., Guerit, L., Rouby, D., & Cordonnier, G. (2019). A New Efficient Method to Solve the  
1190 Stream Power Law Model Taking Into Account Sediment Deposition. *Journal of Geophysical Research:  
1191 Earth Surface*, 124(6), 1346-1365. <https://doi.org/https://doi.org/10.1029/2018JF004867>
- 1192 Zeitler, P. K., Koons, P. O., Bishop, M. P., Chamberlain, C. P., Craw, D., Edwards, M. A., . . . Khattak, M. U. K.  
1193 (2001). Crustal reworking at Nanga Parbat, Pakistan: Metamorphic consequences of thermal - mechanical  
1194 coupling facilitated by erosion. *Tectonics*, 20(5), 712-728.
- 1195 Zeitler, P. K., Meltzer, A. S., Brown, L., Kidd, W. S., Lim, C., & Enkelmann, E. (2014). Tectonics and topographic  
1196 evolution of Namche Barwa and the easternmost Lhasa block, Tibet. In *Toward an improved  
1197 understanding of uplift mechanisms and the elevation history of the Tibetan Plateau* (Vol. 507, pp. 23-58).  
1198 Geological Society of America Special Papers.
- 1199 Zeitler, P. K., Meltzer, A. S., Koons, P. O., Craw, D., Hallet, B., Chamberlain, C. P., . . . Bishop, M. (2001).  
1200 Erosion, Himalayan geodynamics, and the geomorphology of metamorphism. *GSA Today*, 11(1), 4-9.
- 1201 Zhang, H., Hou, Z., Rolland, Y., & Santosh, M. (2022). The cold and hot collisional orogens: Thermal regimes and  
1202 metallogeny of the Alpine versus Himalayan-Tibetan belts. *Ore Geology Reviews*, 141, 104671.
- 1203 Zhang, J., Ji, J., Zhong, D., Ding, L., & He, S. (2004). Structural pattern of eastern Himalayan syntaxis in  
1204 Namjagbarwa and its formation process. *Science in China Series D: Earth Sciences*, 47(2), 138-150.
- 1205 Zhang, Z., Zhao, G., Santosh, M., Wang, J., Dong, X., & Liou, J. (2010). Two stages of granulite facies  
1206 metamorphism in the eastern Himalayan syntaxis, south Tibet: Petrology, zircon geochronology and  
1207 implications for the subduction of Neo - Tethys and the Indian continent beneath Asia. *Journal of  
1208 Metamorphic Geology*, 28(7), 719-733.
- 1209 Zhisheng, A., Kutzbach, J. E., Prell, W. L., & Porter, S. C. (2001). Evolution of Asian monsoons and phased uplift  
1210 of the Himalaya-Tibetan plateau since Late Miocene times. *Nature*, 411(6833), 62-66.
- 1211

## 1212 **References From the Supporting Information**

- 1213 Anders, A. M., Roe, G. H., Hallet, B., Montgomery, D. R., Finnegan, N. J., & Putkonen, J. (2006). Spatial patterns  
1214 of precipitation and topography in the Himalaya. *Special Papers-Geological Society of America*, 398, 39.
- 1215 Bittner, D., & Schmeling, H. (1995). Numerical Modelling of Melting Processes and Induced Diapirism In the  
1216 Lower Crust. *Geophysical Journal International*, 123(1), 59-70. [https://doi.org/10.1111/j.1365-  
1217 246X.1995.tb06661.x](https://doi.org/10.1111/j.1365-246X.1995.tb06661.x)
- 1218 Bookhagen, B., & Burbank, D. W. (2006). Topography, relief, and TRMM - derived rainfall variations along the  
1219 Himalaya. *Geophysical Research Letters*, 33(8).

- 1220 Burg, J.-P., & Gerya, T. V. (2005). The role of viscous heating in Barrovian metamorphism of collisional orogens:  
1221 thermomechanical models and application to the Lepontine Dome in the Central Alps. *Journal of*  
1222 *Metamorphic Geology*, 23(2), 75-95. <https://doi.org/https://doi.org/10.1111/j.1525-1314.2005.00563.x>  
1223 Clauser, C., & Huenges, E. (1995). Thermal conductivity of rocks and minerals. *Rock physics and phase relations: a*  
1224 *handbook of physical constants*, 3, 105-126.
- 1225 Gerya, T. (2019). *Introduction to numerical geodynamic modelling*. Cambridge University Press.
- 1226 Gerya, T. V., & Yuen, D. A. (2003). Rayleigh–Taylor instabilities from hydration and melting propel ‘cold plumes’  
1227 at subduction zones. *Earth and Planetary Science Letters*, 212(1), 47-62.  
1228 [https://doi.org/https://doi.org/10.1016/S0012-821X\(03\)00265-6](https://doi.org/https://doi.org/10.1016/S0012-821X(03)00265-6)
- 1229 Pinkerton, H., & Stevenson, R. J. (1992). Methods of determining the rheological properties of magmas at sub-  
1230 liquidus temperatures. *Journal of Volcanology and Geothermal Research*, 53(1), 47-66.  
1231 [https://doi.org/https://doi.org/10.1016/0377-0273\(92\)90073-M](https://doi.org/https://doi.org/10.1016/0377-0273(92)90073-M)
- 1232 Ranalli, G. (1995). *Rheology of the Earth*. Springer Science & Business Media.
- 1233 Schmidt, M. W., & Poli, S. (1998). Experimentally based water budgets for dehydrating slabs and consequences for  
1234 arc magma generation. *Earth and Planetary Science Letters*, 163(1), 361-379.  
1235 [https://doi.org/https://doi.org/10.1016/S0012-821X\(98\)00142-3](https://doi.org/https://doi.org/10.1016/S0012-821X(98)00142-3)
- 1236 Turcotte, D., & Schubert, G. (2014). *Geodynamics*.
- 1237
- 1238